# Chapter 3

## Role of Cation Deficiency and the Inductive Effect in Ti-Doped NiO for Developing Superior Electrocatalysts for the Oxygen Evolution Reaction

### 3.1 Introduction

The majority of energy sources used today are derived from fossil fuels including natural gas, coal and oil. However, the depletion of finite resources of fossil fuels and the negative environmental repercussions of using fossil fuels has sparked extensive research on innovative technologies for the conversion and storage of clean, sustainable energy sources, such as wind and solar power. [1, 2] Continuous research efforts are being made to investigate new eco-friendly technologies in response to the deterioration of global climate and environment, such as supercapacitors, [3] batteries, [4] photocatalysis, [5] and electrocatalysis, [6] for the application of sustainable and renewable energy sources. [7] The overall electrochemical water splitting is considered a promising approach for energy conversion technologies, which involves two half-reactions: namely the hydrogen evolution reaction (HER) at the cathode and the oxygen evolution reaction (OER) at the anode. OER is kinetically slower than HER as it requires four electrons for the reaction to occur, whereas HER just requires two electrons for the reaction to occur. Thus, the OER is a key process that determines the overall efficiency of electrocatalytic water splitting. Up to now, precious noble metal-based materials such as $IrO_2$ and $RuO_2$ have been considered benchmark electrocatalysts for OER. However, the high cost and low abundance limit their large-scale application. Therefore, it is imperative to explore cost-effective alternative materials that can efficiently reduce the kinetic constraint of OER and enhance the efficacy of water splitting. [8,9] Consequently, a diverse range of transition-metal compounds, such as transition-metal (e.g., Mn, Fe, Co, and Ni) oxides, (oxy)hydroxides, chalcogenides, carbides, phosphides, nitrides and their corresponding composite electrocatalysts have been developed. [10] Due to their low cost, high activity and durability, these materials are regarded as potential alternatives for practical water splitting. [11] In this context, Ni–Fe oxides and (oxy)hydroxides have consistently shown the highest activities and, as a result, have become the most interesting earth-abundant OER catalysts.

[12,13] Recently, it was shown that Ti-doped Ni-Fe oxy-hydroxide ($Ni_xFe_yTi_zOOH$) showed a better OER activity in comparison to $Ni_{0.75}Fe_{0.25}OOH$, a benchmark in the alkaline medium for platinum-group metal-free (PGM-free) catalysts. [10] Materials and electrocatalysts containing titanium have attracted great interest in recent times. [14] Although $TiO_2$ has been widely investigated as an anodic catalytic substance, particularly in a recent study. [15,16] In multimetallic metal oxides (or sulfides), Ti was utilized effectively for enhancing catalytic performance in alkaline media for OER. [14] Recent studies of cobalt-doped black $TiO_2$ nanotube arrays. [17] ultrafine NiO nanosheets supported by $TiO_2$ [18] and Ti−Fe mixed sulfide nanoboxes [19] are of particular relevance for OER in basic media.

NiO-based materials are receiving significant attention due to their low cost, unique chemical properties and good stability. Consequently, this compound has found widespread use in catalytic, gas sensing, magnetic and electrocatalytic materials. [20] As a *p*-type semiconductor, $Ni^{2+}$ vacancies are often present in NiO. [21] The *p*-type conductivity of NiO derives from the presence of two positively charged holes that are associated with each $Ni^{2+}$ vacancy in the lattice. According to the Kroger–Vink notation $1/2\ O_2(g) \leftrightarrow O_O^x + V_{Ni}'' + 2\ h^+$ in which $V_{Ni}''$ denotes $Ni^{2+}$ vacancy and $O_O^x$ denotes oxygen atom located on the lattice site of NiO. [22] For charge neutrality, the two $h^+$ will be neutralized by increasing the valence states of the two neighboring $Ni^{2+}$ to $Ni^{3+}$ ($Ni^{2+} + h^+ \rightarrow Ni^{3+}$) or by increasing the valence states of the two neighboring $O^{2-}$ to $O^-$ ($O^{2-} + h^+ \rightarrow O^-$). A thorough understanding of the role of defects in electrocatalysts is crucial for guiding the rational design of defects in catalysts to achieve optimal HER [23,24] and OER activity. [25-27]

In the present work, we investigate defect chemistry when Ni and Ti coexist in the crystal structure since prior research has shown that atom vacancies can significantly increase catalytic

activity. [28-30] Specifically, when both Ti and Ni are present in the same crystal structure in the composition of $Ni_{1-2x}Ti_xO$ , their distinct oxidation states of 4+ for Ti and 2+/3+ for Ni result in the formation of cation vacancies to maintain charge neutrality with oxygen [given as $NiO + Ti = Ni_{1-2x}Ti_xV_x''O$ where $V_x''$ denotes the cationic vacancy].

The inductive effect, which arises from differences in electronegativity, is prevalent in multicomponent materials. Substituents/components with more electronegativity tend to pull the electron cloud of chemical bonds, thus resulting in the tuned surface electronic structure of catalysts. [31] The incorporation of foreign metal substituents to tune the redox potential has been proven to be a very effective method to improve the performance of oxygen electrocatalysis. [32,33] Herein, a series of cubic rock salt structure compounds $Ni_{1-2x}Ti_xV_x''O$ ($x$ = 0.03, 0.05, 0.075, 0.1) have been synthesized by the sol−gel route to investigate the influence of the composition on electrochemical activity toward the oxygen evolution reaction (OER). Cationic vacancy and the inductive effect brought about by the $Ti^{4+}$ at the Ni site in rock salt NiO lattice results in the enhancement of OER activity. The result corroborates with the findings of recent investigations on $Bi_{0.2}Sr_{0.8}CoO_{3-\delta}$,[34] Ti-doping in $Fe_2O_3$, [35] Co-vacancy-rich $Co_{1-x}S$ [25] and layered $Li_{1-x}Cr_{1-x}Al_xO_2$. [36] From linear sweep voltammograms (LSV) results, we found that titanium doping in $Ni_{1-2x}Ti_xV_x''O$ ($0 \leq x \leq 0.1$) increases the OER activity and the best OER activity is achieved for $Ni_{0.9}Ti_{0.05}O$ with a Tafel slope of 67 mV $dec^{-1}$ and an overpotential of 304 mV at a current density of 10 mA $cm^{-2}$, comparable to that of the commercial $RuO_2$ benchmark catalyst, measured under similar experimental conditions.

## 3.2 Experimental Section

### 3.2.1 Material Synthesis

A sol-gel synthesis route was utilized to synthesize polycrystalline $Ni_{1-2x}Ti_xO$ ($x$ = 0.03, 0.05, 0.075, 0.1) powder sample. Stoichiometric quantity of precursor compounds such as $Ni(NO_3)_2.6H_2O$ (Sigma Aldrich, ≥ 99 %), $(C_3H_7O)_4Ti$, titanium isopropoxide (TIP) (Sigma Aldrich, ≥ 98 %), were used as received without further purification. Double-distilled (DD) water was used during all of the experimental processes. A stoichiometric amount of $Ni(NO_3)_2.6H_2O$ was dissolved in 20 mL (DD) water and 10 mL of ethylene glycol solution, referred to as solution A. The mixture was stirred for half an hour at 80 ℃ on a hot plate. In 5 mL of cold $HNO_3$, the stoichiometrically calculated amount of TIP was added and stirred to get a clear solution followed by adding it to the above solution A. Then the reaction was continued for 6 h with stirring at 80 ℃. The sample mixture was initially heated at 400 ℃ for 1 h and then calcined at 500 ℃ for 6 h in an oxygen environment with an intermediate grinding step to get single-phase material. The series of $Ni_{1-2x}Ti_xO$ samples were denoted as NTO-0, NTO-3, NTO-5, NTO-7.5 and NTO-10 for x = 0, 0.03, 0.05, 0.075, 0.1, respectively, in this manuscript. The electrochemical activity of the synthesized catalyst was compared with commercial $RuO_2$ (Sigma Aldrich, 99%, a well-known benchmark catalyst for oxygen evolution reaction) in the same condition of the experiment.

## 3.3 Result and Discussion

### 3.3.1 XRD Studies and Rietveld Refinement

The well-separated diffraction peaks of the $Ni_{1-2x}Ti_xO$ ($x$ = 0, 0.03, 0.05, 0.075, 0.1) samples in the XRD patterns, in **Figure 3.1 a**, are indicative of the material's crystalline form and are well-indexed with the standard cubic phase space group: *Fm-3m* (225) of NiO (JCPDS No. 47-1049). No impurity peaks were identified up to 7.5% Ti doping in the $Ni_{1-2x}Ti_xO$ structure. However, a

small impurity peak of $NiTiO_3$ appeared at 10% dopant concentration. It is evident from the XRD pattern that on increasing the doping percentage of Ti in $Ni_{1-2x}Ti_xO$ , the intensity count decreases and the peak broadening increases. The magnification of the highest intensity peak, (200), at $2\theta$ = ~43° exhibits broadening and slight shifting toward higher angle with increasing dopant concentration (**Figure 3.1b**) confirming the incorporation of Ti in the NiO lattice. Further to understand the effect of doping on the crystallite size, we calculated the crystallite size using the Debye– Scherrer equation: $D = 0.9\lambda/\beta cos\theta$ (3.1)

where $D$ is crystallite size, $\lambda$ is the wavelength of the X-ray radiation (1.54 Å for Cu Kα), $\beta$ is the full-width half maxima and θ is the diffraction angle, was used to calculate crystallite size. [37] The average crystallite size was found to decrease from ~9.9 (±1) to ~6.9 (±1) nm with increasing doping percentage of Ti. Further, Rietveld refinement of all NTO samples was performed by taking Pseudo-Voigt as peak profile function and *Fm-3m* space group, shown in **Figure 3.2**.

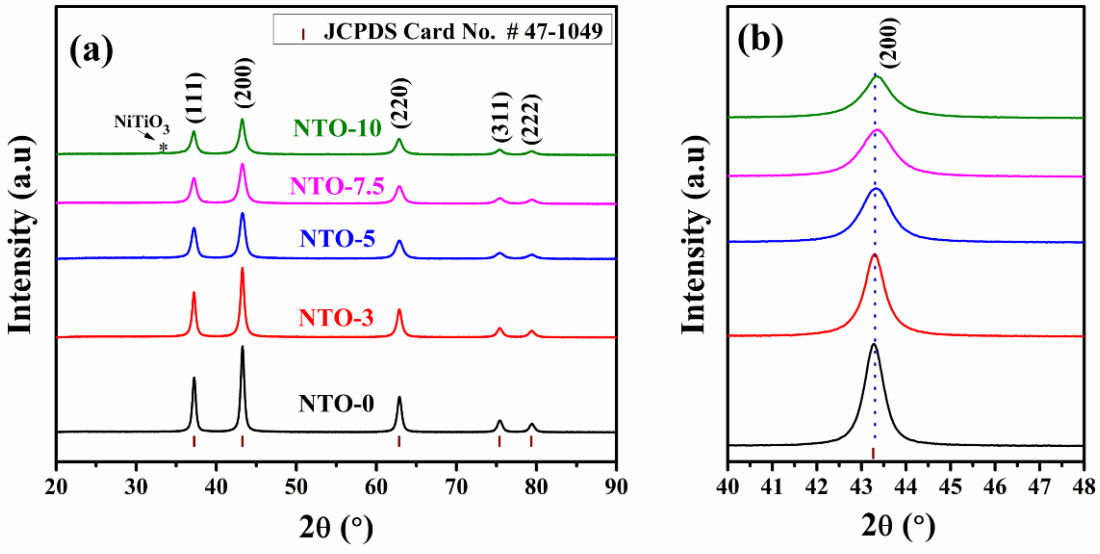


**Figure 3.1 (a)** XRD pattern of all sol-gel synthesized NTO samples and **(b)** Magnified image of (200) peak.

The refinement results along with their reliability factors ($R_{bragg}$, $R_f$ and $\chi^2$) were listed in **Table 3.1**. It is clear from the refinement results (**Table 3.1)** that the lattice parameter slightly decreases in comparison with the pure NiO because $Ti^{4+}$ has a smaller ionic radius (0.60 Å) than $Ni^{2+}$ (0.69 Å).

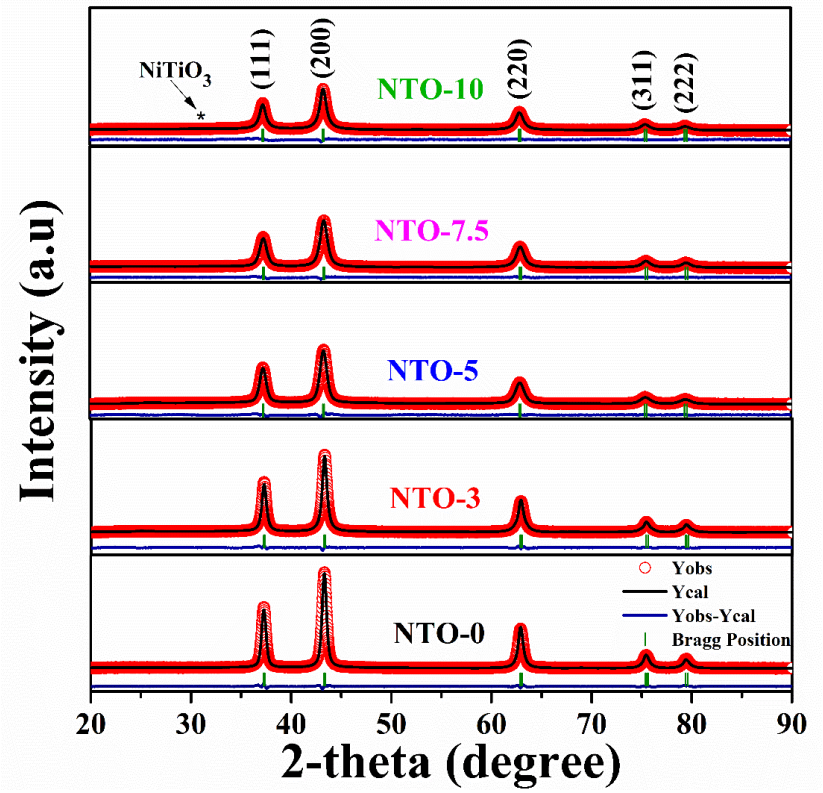


**Figure 3.2** Rietveld refined powder XRD patterns of all NTO samples.

**Table 3.1** Rietveld refined structural parameters of NTO-0, NTO-3, NTO-5, NTO-7.5 and NTO-10.

| Samples | a =b=c (Å) | α = β = γ | V (Å)$^3$ | Rp | Rwp | $\chi^2$ |
|---|---|---|---|---|---|---|
| NTO-0 | 4.178(2) | 90° | 72.94(3) | 5.87 | 4.84 | 2.01 |
| NTO-3 | 4.178(7) | 90° | 72.93(7) | 6.21 | 5.32 | 2.40 |
| NTO-5 | 4.177(3) | 90° | 72.85(3) | 7.65 | 5.92 | 2.42 |
| NTO-7.5 | 4.176(4) | 90° | 72.83(1) | 7.73 | 5.83 | 2.67 |
| NTO-10 | 4.175(6) | 90° | 72.78(6) | 9.48 | 7.76 | 2.89 |

### 3.3.2 Raman Analysis

The structural formation and phase purity of NiO and Ti-doped NTO samples were further confirmed by the Raman study. Room temperature Raman spectra of all the NTO samples recorded in the range between 1400–200 $cm^{-1}$ shown in **Figure 3.3 a**. The spectra show two main peaks identified at approximately 515 $cm^{-1}$ and 1060 $cm^{-1}$. The strong peak around 515 $cm^{-1}$ corresponds to a first-order longitudinal–optical one-phonon (1P) mode of 1LO peak associated with the vibrations of Ni–O. The broader peak around 1060 $cm^{-1}$ is due to a second-order longitudinal–optical two-phonon (2P) mode of 2LO peak. There is a second-order transverse optical phonon mode 2TO at ~704$cm^{-1}$. Other modes, such as the 1TO at approximately 367 $cm^{-1}$ and LO+TO at around 896 $cm^{-1}$ have lower intensity in the spectra. These modes correspond to the stretching vibrations of NiO. [38,39] The 1LO mode is shifted towards lower wavenumber for Ti-doped NiO indicates the increase in the Ni-O bond length due to addition of Ti in the NiO host lattice. [38] The presence of dominant 1LO, 1TO and its overtones can be attributed to the lattice distortion induced by $Ni^{2+}$ vacancies in NTO. To understand the degree of distortion in NTOs due to $Ni^{2+}$ vacancies, the intensity ratio of first-order and second-order optical phonon vibrations ($I_{1LO}/I_{2LO}$) is plotted in **Figure 3.3 b**. It can be seen that the $I_{1LO}/I_{2LO}$ increases with increasing doping percentage of Ti in NiO. It means that the $Ni^{2+}$ vacancies in the lattice gradually increases with Ti doping. [40, 41] The Raman spectra show no impurity peaks, confirming the purity and cubic phase of the samples. This observation is consistent with the findings from XRD analysis.

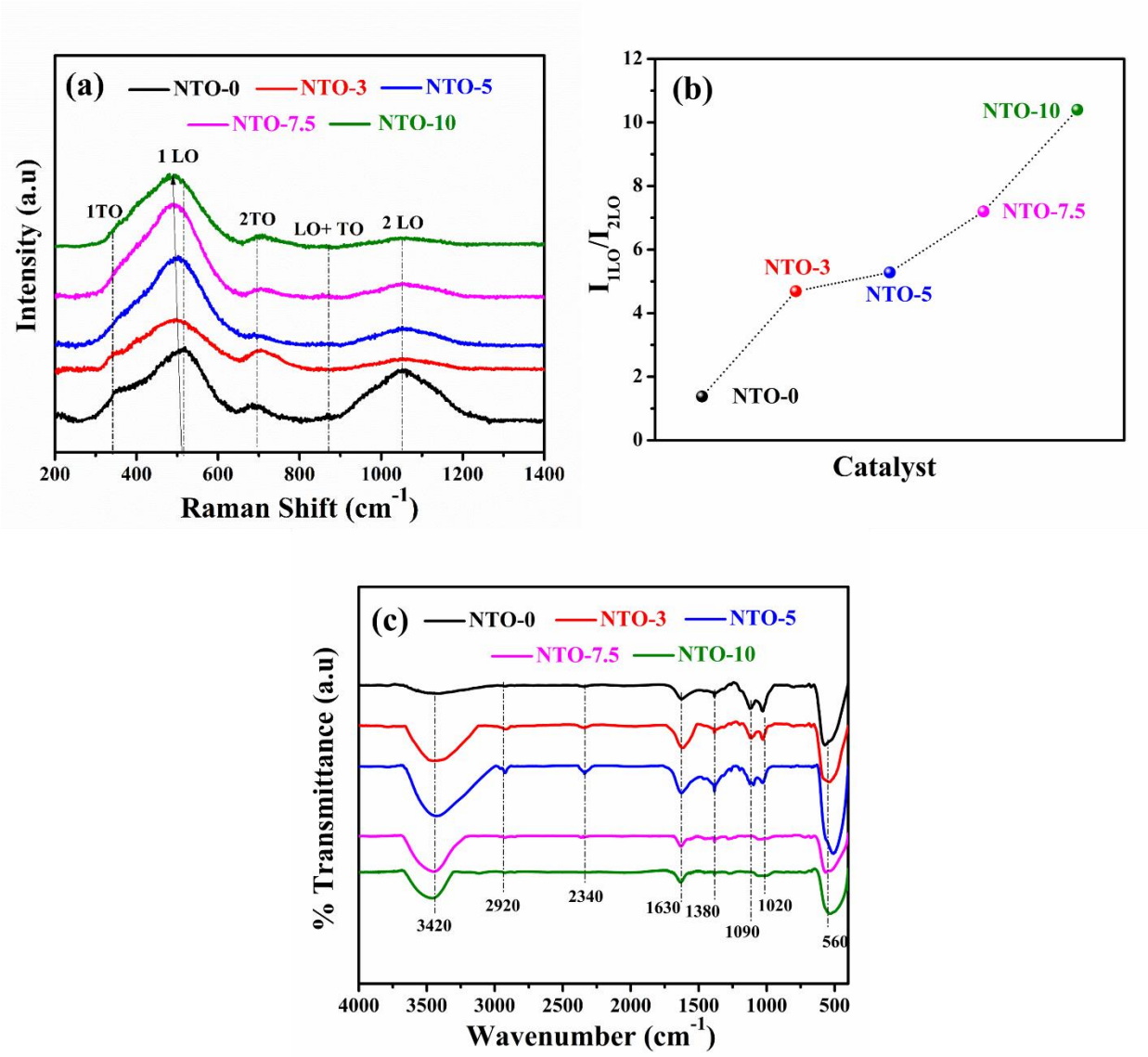


**Figure 3.3. (a)** Room temperature Raman spectra of all the NTO samples, **(b)** intensity ratio of first-order and second-order optical phonon vibrations ($I_{1LO}/I_{2LO}$) varying with NTO samples and **(c)** FTIR spectra of NTO-0 and NTO-5 samples.

### 3.3.3 FT-IR Analysis

FT-IR spectroscopy is employed to examine the vibrational bands of NTO-0 and the modifications resulting from Ti doping in NTO-0 structure. FT-IR spectra of pure NTO-0 and all the doped NTO-3 to NTO-10 samples are recorded in the range between 4000–400 $cm^{-1}$ shown in **Figure 3.3 c**. The broad band around 3420, 1630 and 1380 $cm^{-1}$ are assigned to stretching and bending vibrations

of the –OH group absorbed on the catalyst surface from the atmosphere during the analysis. [42] The absorption bands at 2340 and 2920 $cm^{-1}$ are assigned to the symmetric /asymmetric stretching vibration modes of the absorbed $CO_2$ and C–H bond stretching respectively. [43] The peak around 1020 $cm^{-1}$ and 1090 $cm^{-1}$ in all samples can be attributed to the carbonate groups, which originate from the reaction of the samples with $CO_2$ from air during the analysis procedure. The peak appearing at 560 $cm^{-1}$ in the NTO-0 sample is due to the Ni–O bond [44] and a shift to lower frequency is observed on Ti doping in the NTO samples, when compared to NTO-0, which confirms the weakening of the Ni–O bond on doping. [45] The difference in ionic radii between $Ni^{2+}$ and $Ti^{4+}$ results in the shift in frequencies between the spectra. This further validates that Ti has been successfully doped within the NiO crystal lattice. The shift of Ni–O stretching frequency to lower value confirms the weakening of the Ni–O bond which supports the enhancement of the catalytic activity of the material. The best activity of NTO-5 is related with optimum number of active sites and cation vacancy. As doping beyond 5% also leads to decrease in the active site $Ni^{2+}/Ni^{3+}$.

### 3.3.4 XPS and ICP Analysis

XPS experiments were carried out to confirm the electronic state of the elements (Ni, Ti and O) in NTO-0 and NTO-5 samples (the survey spectra shown in **Figure 3.4 (a, b)**. For precise determination of the double peak characteristics of Ni ($2p_{1/2}$) and Ni ($2p_{3/2}$), the XPS spectrum **Figure 3.5 (a, b)**, were deconvoluted using Voigt peak function and the Shirley background with the XPS Peak41 software. The Ni 2*p* signals at 854.3 and 871.6 eV are attributed to $2p_{3/2}$ and $2p_{1/2}$ of $Ni^{2+}$, and at 856.4 and 873.5 eV to $2p_{3/2}$ and $2p_{1/2}$ of $Ni^{3+}$. The additional peaks located at around 861.4, 865.6, 876.8 and 880.5 eV are matched to their respective satellite peaks. [46]

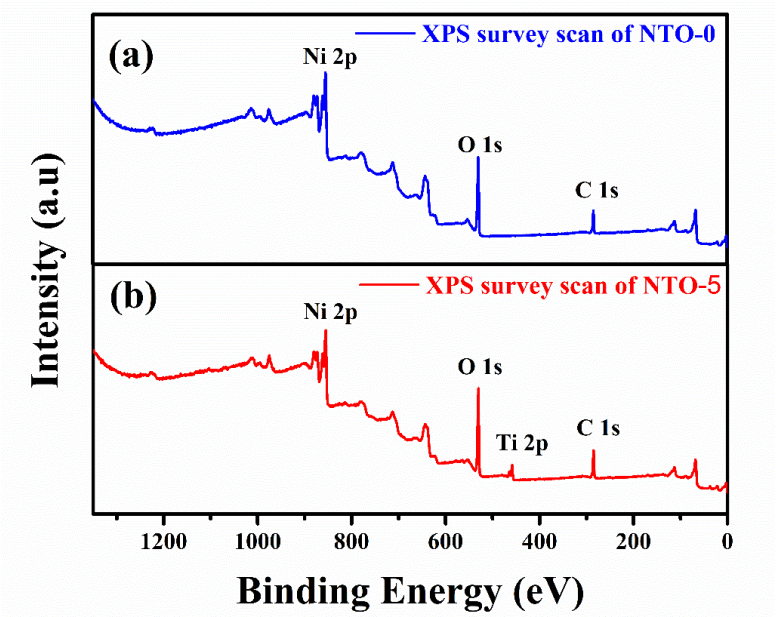


**Figure 3.4** XPS full survey scan of **(a)** NTO-0 and **(b)** NTO-5 sample.

These findings verify that the peak positions are similar to those reported in previous studies for $Ni^{2+}$ and $Ni^{3+}$ oxidation states in stoichiometric and non-stoichiometric NiO. [47, 48] After deconvolution, the observed ratio between the fractional composition of $Ni^{2+}$: $Ni^{3+}$ in NTO-0 was 0.75:0.25, which on Ti doping changes to $Ni^{2+}$:$Ni^{3+}$ :: 0.58:0.42. This confirms that $Ti^{4+}$ doping in NiO is tuning the $Ni^{3+}$ concentration in the NiO lattice. Further, the Ni $2p_{3/2}$ peak shifted by around 0.5 eV from 854.3 eV to 854.8 eV and Ni $2p_{1/2}$ peak shifted by around 0.6 eV from 871.6 to 872.2 eV in the NTO-5 sample compared to the NTO-0 sample (no Ti-doped sample). This shift confirms that the doping of more electronegative $Ti^{4+}$ ions into the lattice increases the ionicity of the Ni–O bond through the inductive effect along with resulting in a high concentration of $Ni^{3+}$ ions in the lattice. [36, 49]

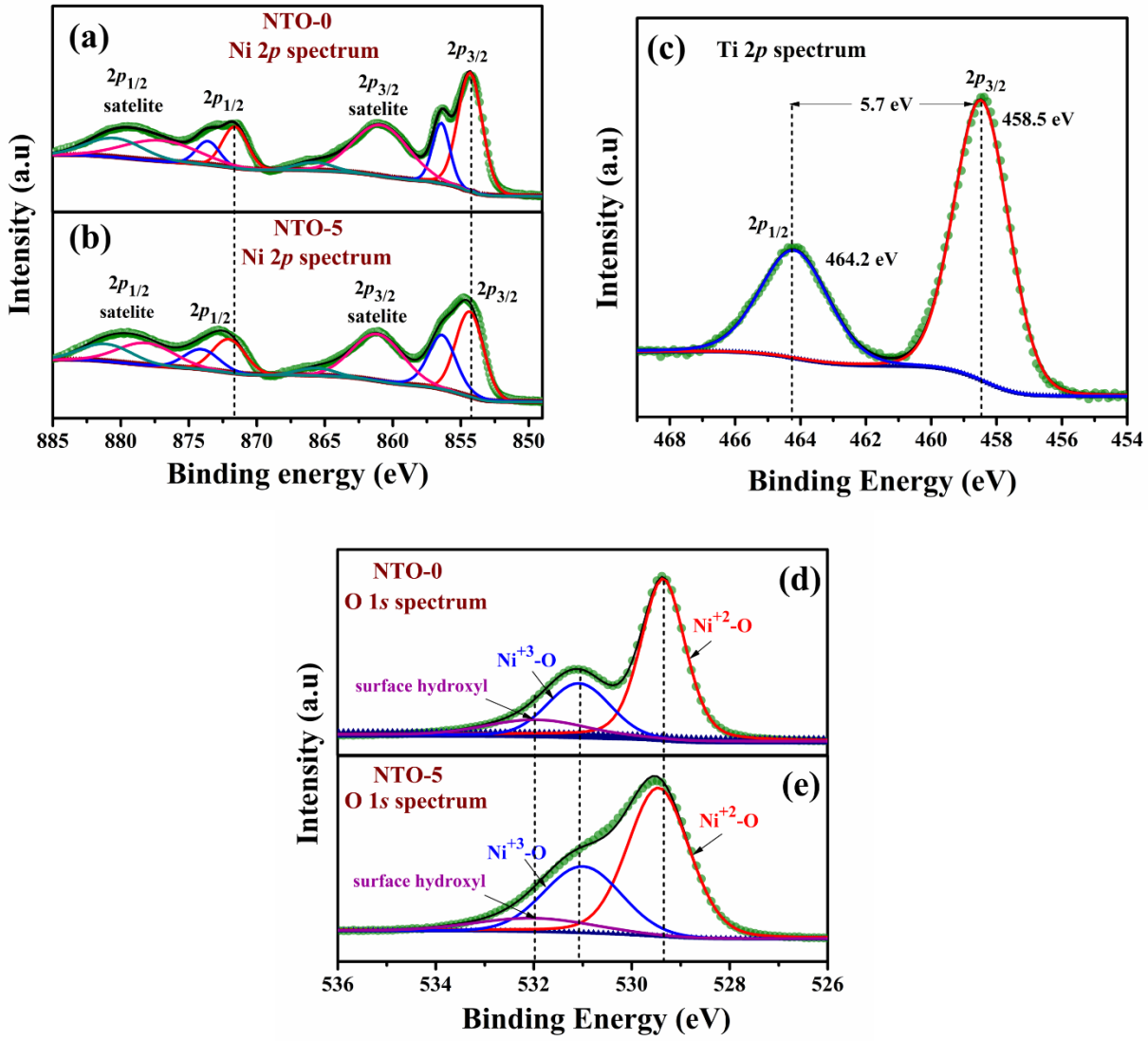


**Figure 3.5**. Core level XPS spectrum of **(a), (b)** Ni (2p), **(c)** Ti (2p), **(d), (e)** O (1s).

The Ti 2*p* core-level spectrum of NTO-5, in **Figure 3.5c**, consists of two peaks centered at 464.2 and 458.5 eV corresponding to Ti ($2p_{1/2}$) and Ti ($2p_{3/2}$), confirming that Ti is present in the +4-oxidation state. [50, 51] The O 1*s* spectrum of NTO-0, NTO-5 shown in **Figure 3.5d** and **Figure 3.5e** respectively, was deconvoluted into three peaks. The peaks at 532.1, 529.3 and 531.1 eV correspond to surface hydroxyl and oxygen bonds with $Ni^{2+}$ and $Ni^{3+}$ respectively, for NTO-0 and

NTO-5. Followed by the electronic state of the elements, the XRD, FT-IR and Raman studies confirms the formation of cation vacant $Ni_{1-2x}Ti_xV_x''O$ cubic lattice.

An estimation of the relative surface concentrations of Ni and Ti in both the prepared catalysts NTO-0 and NTO-5 was conducted by using the following formula. [52]

$$Relative\ concentration, C_M = \frac{I_M/\lambda_M\sigma_M D_M}{\sum(I_M/\lambda_M\sigma_M D_M)} \quad (3.2)$$

where $I_M$ is the integrated intensity of the core levels (M = Ni 2*p* and Ti 2*p*), $\lambda_M$ is the mean escape depths of the respective photoelectrons, $\sigma_M$ is the photoionization cross section, and $D_M$ is the geometric factor. The photoionization cross-section values were taken from Scofield's data [53] and the mean escape depths were taken from Penn's data. [54] The geometric factor was taken as 1 because the maximum intensity in this spectrometer is obtained at 90°. The surface concentrations of Ni/Ti were found in the ratio of 0.9:0.05 in $Ni_{0.9}Ti_{0.05}O$. Further, the relative concentrations of Ni and Ti in the samples were also examined by the ICP analysis using inductively coupled plasma mass spectrometry (ICP−MS), (make:Agilent7800ICP−MS mainframe).The nominal (desired) and actual (obtained from the ICP−MS analysis) compositions of all synthesized $Ni_{1-2x}Ti_xV_x''O$ (x = 0, 0.03, 0.05, 0.075, 0.1) catalysts are listed in **Table 3.2**.The observed value from the XPS study matches very well with the elemental ratios obtained from the ICP−MS study. Thus, the formula of the compound along with their electronic structure can be represented as $Ni_{0.9}Ti_{0.05}O$.

### 3.3.5 Microstructural Analysis

The surface morphology and particle size distribution of the NTO-0 and NTO-5 samples were studied from the scanning electron micrographs. The HR-SEM image of the NTO-0 and NTO-5 sample shown in **Figure 3.6(a-d)** depicts the uniform and homogeneous agglomerated particles,

and its size ranges from 100 to 200 nm distributed in the entire region of the micrograph. The elemental colour mapping of the NTO-0 and NTO-5 sample shown in **Figure 3.6e** and **Figure 3.6f** respectively, confirms the homogeneous distribution of the element in the samples. The energy-dispersive spectrum of NTO-0 (**Figure 3.6g**) and NTO-5 (**Figure 3.6h**) confirms the presence of Ni, Ti and O in their respective samples.

**Table 3.2** Relative concentration of Ni and Ti in $Ni_{1-2x}Ti_xO$ (x = 0, 0.03, 0.05, 0.075, 0.10) from ICP analysis.

| **Catalyst** | **Nominal Composition** | **ICP composition of $Ni_{1-2x}Ti_xO$ ($x$ = 0, 0.03, 0.05, 0.075, 0.10)** | |
|---|---|---|---|
| | | **Ni** | **Ti** |
| **NTO-3** | $Ni_{0.94}Ti_{0.03}O$ | 0.94 | 0.03 |
| **NTO-5** | $Ni_{0.9}Ti_{0.05}O$ | 0.90 | 0.05 |
| **NTO-7.5** | $Ni_{0.85}Ti_{0.075}O$ | 0.85 | 0.075 |
| **NTO-10** | $Ni_{0.8}Ti_{0.10}O$ | 0.80 | 0.10 |

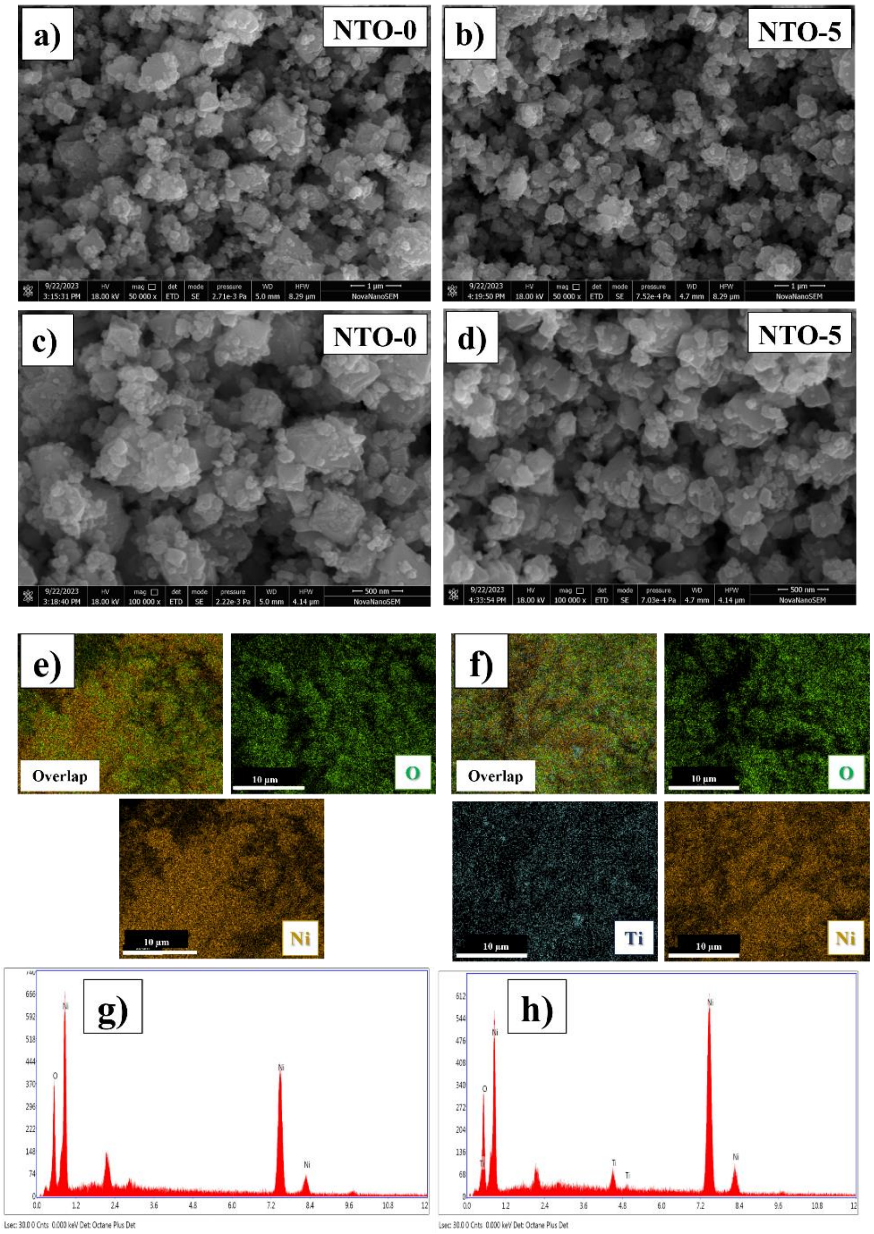


**Figure 3.6.** SEM micrograph of **(a), (c)** NTO-0 **(**the scale bars are 1 μm and 500 nm respectively), **(b)**, **(d)** NTO-5 (the scale bars are 1 μm and 500 nm respectively), **(e)**, **(f)** represents elemental mapping of individual elements (Ni, Ti, and O) present in the NTO-0 and NTO-5 sample and **(g)**, **(h)** EDX spectrum of NTO-0, NTO-5.

Bright-field TEM images of the NTO-0 and NTO-5 sample (in **Figure 3.7a**, **d**) indicates irregular aggregated particles. The high-resolution–TEM images, **Figure 3.7b**, **e** presents the lattice arrangements at the localized region of the powder sample. The lattice fringes of the NTO-0 and

NTO-5 samples shown in **Figure 3.7c**, **f** corresponds to the (200) and (111) plane. The HRTEM results reveals that interplanar *d*-spacing for both the samples follows the sequence NTO-0 > NTO-5 which is in accordance with the XRD result. Also, selected-area electron diffraction (SAED) shows the concentric diffraction rings, in inset of **Figure 3.7b, e** which further indicates the crystalline nature of both the samples. The interplanar distances measured from the SAED pattern show good agreement with the cubic NiO. The diffraction rings are indexed to (111), (200), (220), (311) and (222) from the inside to the outside matches well with the XRD results.

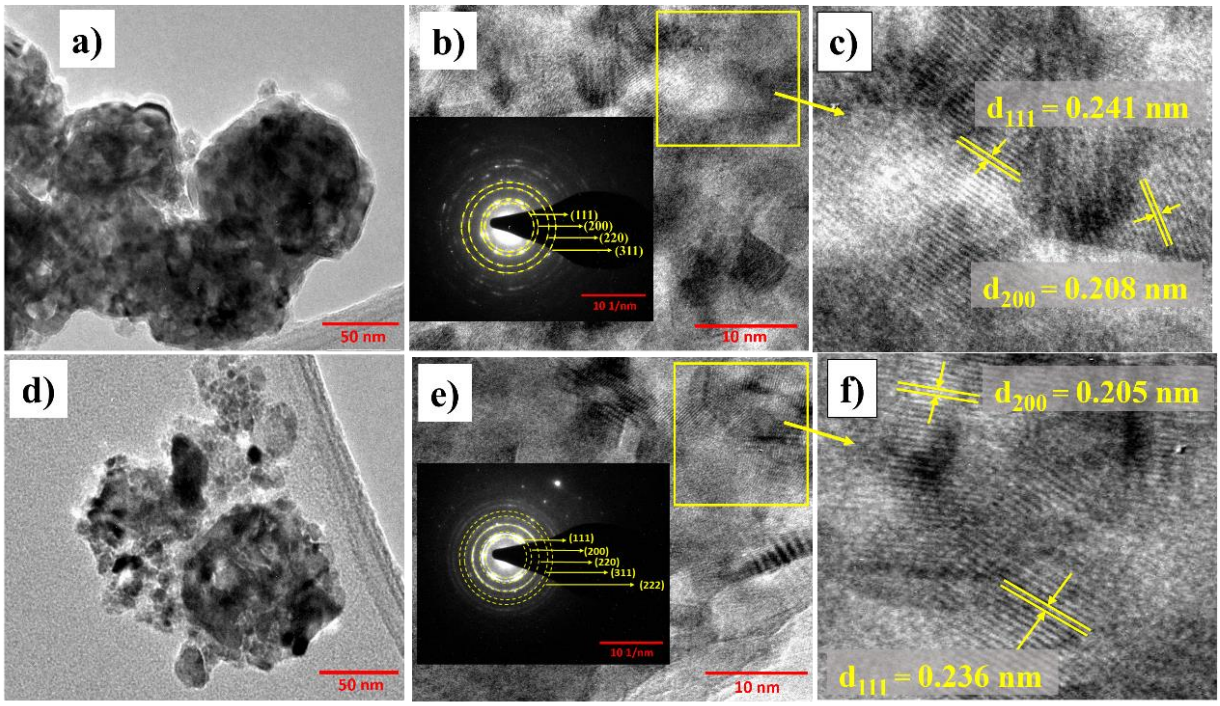


**Figure 3.7.** Bright-field TEM image **(a)** NTO-0, **(d)** NTO-5, **(b), (e)** HR-TEM image lattice arrangements at the localized region for NTO-0 and NTO-5; inset shows the respective SAED patterns and **(c, f)** HR-TEM image with interplanar d-spacing of (200) and (111) plane for NTO-0 and NTO-5 respectively.

### 3.3.6 Electrochemical Studies

#### 3.3.6.1 OER Performances of Synthesized Catalysts

The electrochemical performance of $Ni_{1-2x}Ti_xO$ ($0 \leq x \leq 0.1$) catalysts toward the OER was investigated in $O_2$-saturated 1 M KOH at a scan rate of 5 mV $s^{-1}$ in a three-electrode setup. Several cycles of fast scan CV were performed on the working electrode before collecting the data in the range of 1.0 to 1.8 V *vs* RHE to obtain a stable current. The LSV curves, in **Figure 3.8a,** show the OER performances of all the synthesized NTO catalysts follow the order NTO-10 < NTO-0 < NTO-7.5 < NTO-3 < NTO-5. OER activity reaches its optimum performance for 5% Ti doping and the activity decreases with further increase in the dopant concentration. Inset of **Figure 3.8a** highlights the 1.2–1.6 V LSV region, with a ~1.4 V peak confirming $Ni^{2+}/Ni^{3+}$ as the active species, detailed in **Figure 3.12**. The overpotential required to achieve the current density of 10 mA $cm^{-2}$ for NTO-0-10 samples was found to be 358, 322, 304, 334 and 392 mV, respectively, shown in **Figure 3.8b**. Tafel analysis is one of the primary studies in the evaluation of electrocatalysts for water electrolysis. It depicts the relationship between potential and logarithm of current density, is an important factor in assessing the reaction kinetics. **Figure 3.8c** shows the Tafel plot of a series of $Ni_{1-2x}Ti_xO$ samples and the Tafel slope values obtained for NTO-0, NTO-3, NTO-5, NTO-7.5 and NTO-10 are approximately 82, 78, 67, 71 and 95 mV $dec^{-1}$, respectively. A low Tafel slope value is an indication of a good electrocatalyst with decreasing overpotential. The lowest Tafel value of NTO-5 (67 mV $dec^{-1}$) indicates its faster reaction kinetics compared to all other Ti-doped NiO catalysts. EIS measurements were also performed to determine the charge-transfer resistance $R_{ct}$ of all the catalysts. Impedance studies for the catalysts $Ni_{1-2x}Ti_xO$ were conducted in the frequency range of 10 Hz – 100 kHz with an AC amplitude of 10 mV at a potential of 1.5 V *vs* RHE, as shown in **Figure 3.8d**. where the inset shows; an equivalent circuit fit of the EIS data, the solution resistance ($R_s$), charge-transfer resistance ($R_{ct}$) and double-layer capacitance

($R_{Cdl}$). The charge transfer resistance ($R_{ct}$) (diameter of the semicircle in the Nyquist plot at the high-frequency region) is linked with the electrochemical kinetics of the reaction. A smaller semicircle loop suggests lower charge-transfer resistance and a sign of faster kinetics during the OER process. [55] The $R_{ct}$ value of NTO-5 is found to be 9.02 Ω, which is lower than all other synthesized catalysts NTO-0 (12.72 Ω), NTO-3 (10.77 Ω), NTO-7.5 (11.72 Ω) and NTO-10 (18.02 Ω), indicating its faster OER kinetics rate compared to the other catalysts.

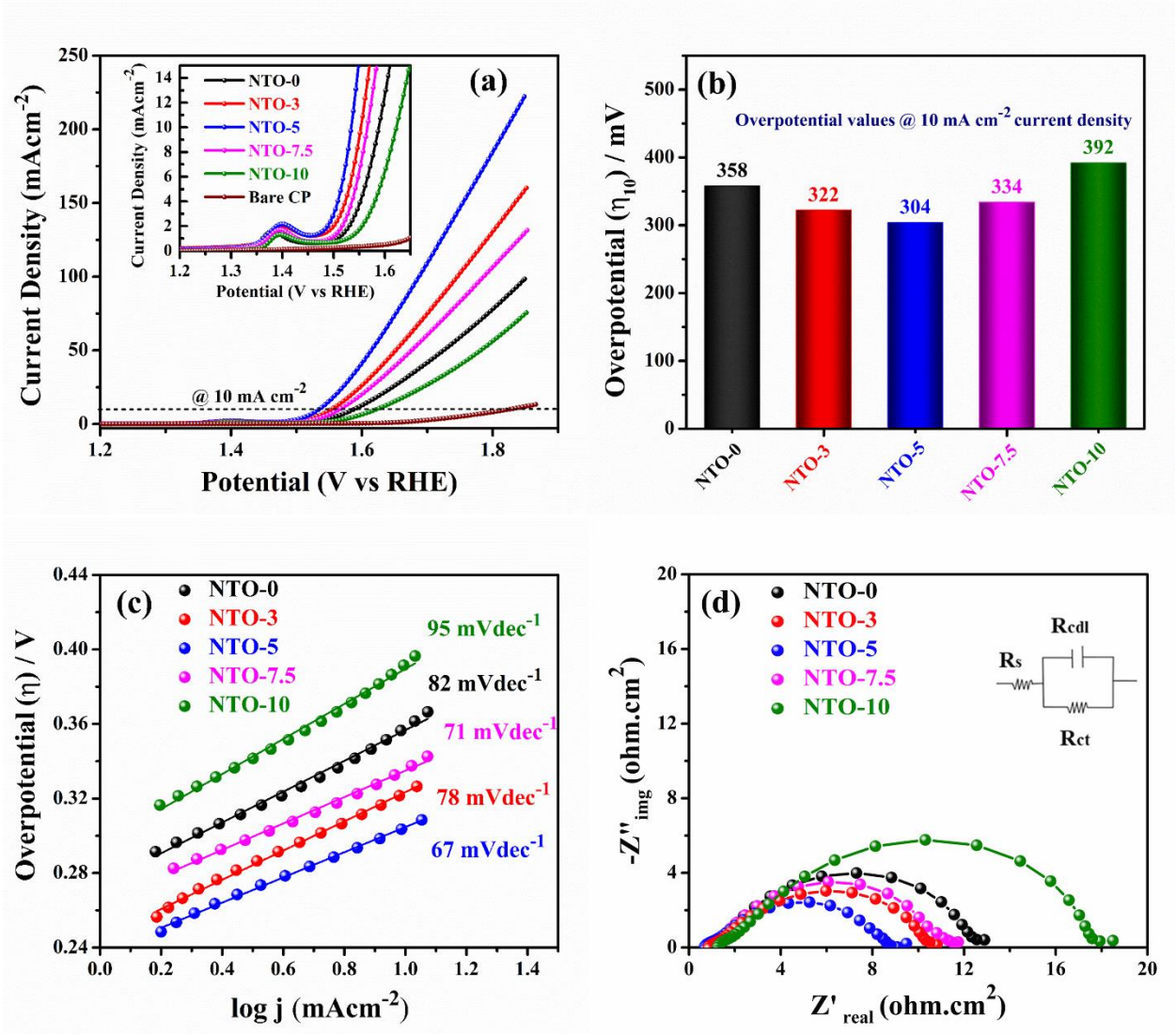


**Figure 3.8.** OER performance of NTO series samples $Ni_{1-2x}Ti_xO$ (x = 0.03, 0.05, 0.075, 0.1). **(a)** Linear sweep voltammograms taken at a scan rate of 5 mV $s^{-1}$ in 1 M KOH, **(b)** Overpotentials at a current density of 10 mA $cm^{-2}$, **(c)** Tafel plots & **(d)** EIS recorded at 1.54 V vs. RHE.

The OER performance of NTO-5 was conducted in different pH concentration of 0.1, 0.5, 1 and 2 M KOH electrolytes (with pH ranging from 13-14.3) as shown in **Figure 3.9**, and found that NTO-5 have a noticeable pH-dependent OER activity. The activity of NTO-5 increases with KOH electrolyte concentration up to 1 M; however, beyond 1 M KOH electrolyte, the OER performance dropped. This may be due to the fact that all adsorption sites were filled by $OH^-$ at a lower concentration (up to 1 M).

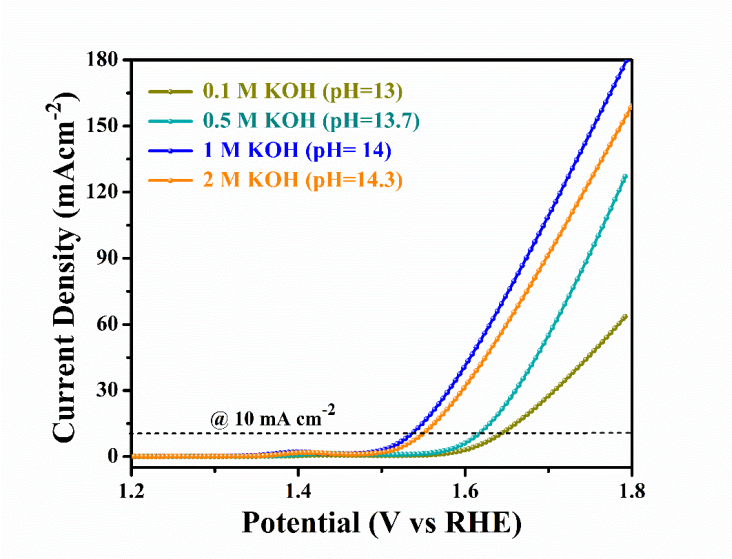


**Figure 3.9** OER performance of the NTO-5 catalyst in different concentration of KOH electrolyte with pH ranging from 13 to 14.3.

Furthermore, to examine the intrinsic properties of the electrocatalyst, the electrochemically active surface area (ECSA) of each catalyst was calculated via double-layer capacitance measurement. The double-layer capacitance ($C_{dl}$) is analyzed by CV in a non-faradic potential range from 0.86 to 0.96 V with different scan rates ranging from 40 to 140 mV/s, as shown in **Figure 3.10 (a-e)**. The change in current density ($\Delta J$) for anodic and cathodic scans in CV depends on the charge-storing ability of the working electrode and it increases linearly upon increasing the scan rate.

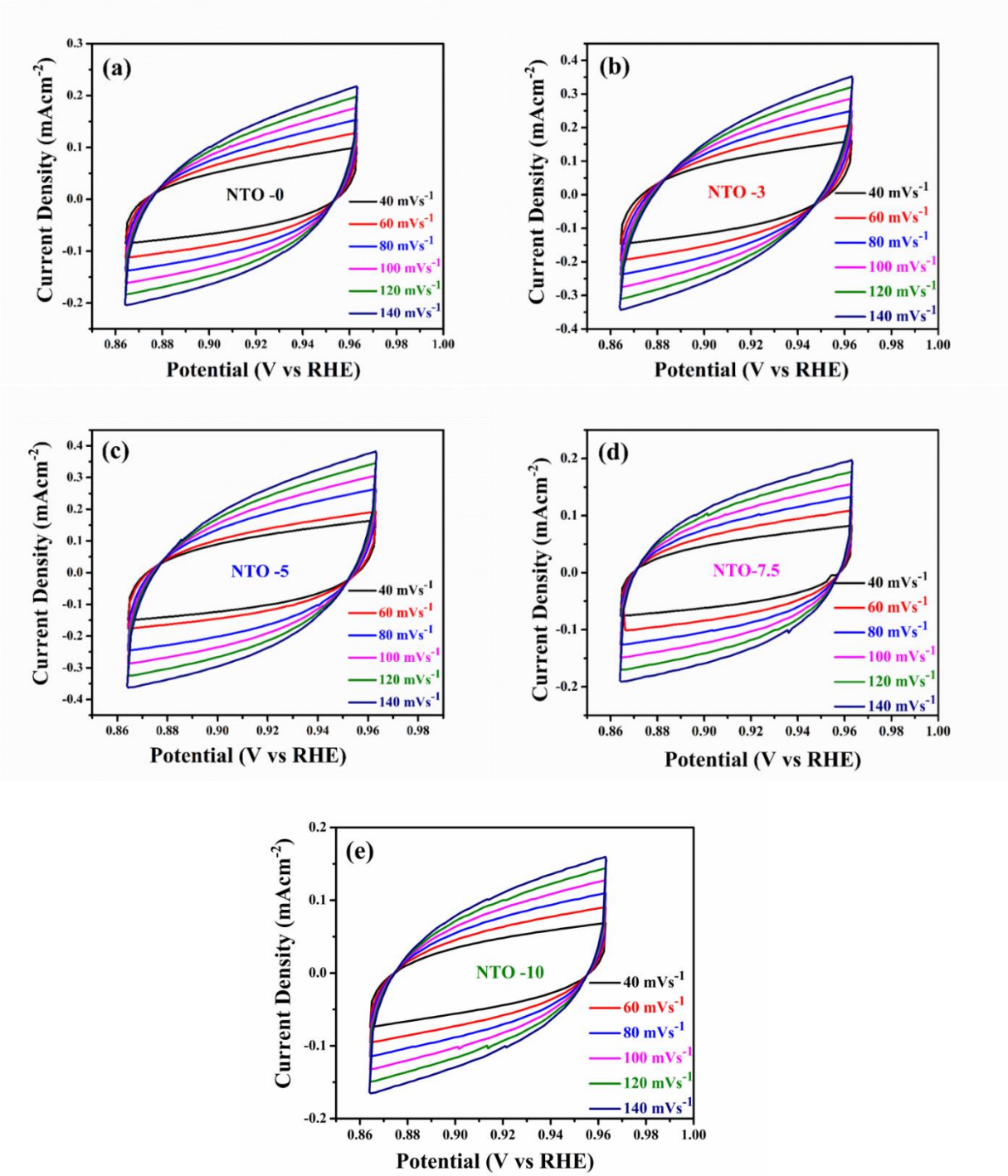


**Figure 3.10** CV measurements in a non-faradic current region (0.86 – 0.96 V vs. RHE) at scan rates of 40, 60, 80, 100, 120 and 140 mV $s^{-1}$ of **(a)** NTO-0, **(b)** NTO-3, **(c)** NTO-5**, (d)** NTO-7.5 & **(e)** NTO-10 in 1 M KOH.

The double layer capacitance which is the slope of $\Delta J/2$ *vs* η plot is found to be 0.89, 1.12, 1.25, 1.91, 2.24 mF/cm$^{-2}$ for all the NTO series catalysts, following the order NTO-10 < NTO-0 < NTO-7.5 < NTO-3 < NTO-5 as plotted (**Figure 3.11a**) for each catalyst.

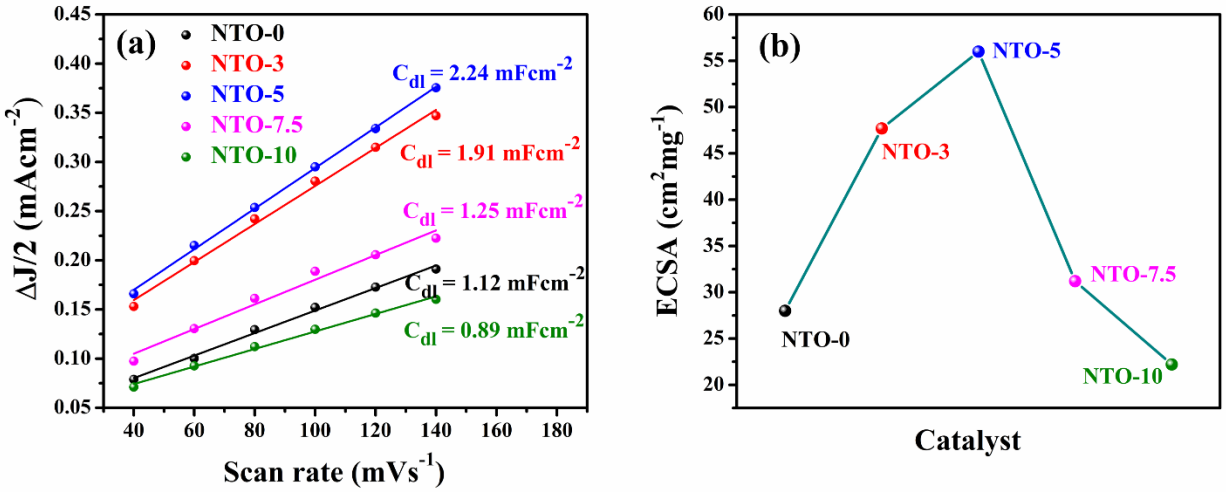


**Figure 3.11.** OER performance of NTO series samples $Ni_{1-2x}Ti_xO$ (x = 0.03, 0.05, 0.075, 0.1). **(a)** Plots of capacitive current density differences ΔJ/2 vs. the scan rate for all NTO samples & **(b)** Plot of ECSA vs catalyst $Ni_{1-2x}Ti_xO$ (x = 0.03, 0.05, 0.075, 0.1).

The best electrocatalytic OER activity was obtained for NTO-5 or up to 5% Ti doping in NiO and OER activity decreases with further increase in Ti substitution at the Ni site in NiO rock-salt lattice as higher Ti substitution effectively decreases the active site ($Ni^{2+/3+}$) participation for the reaction on surfaces due to increase in cation vacancies and non-active smaller size $Ti^{4+}$ at surfaces.

The ECSA of a catalyst is determined by using the double-layer capacitance according to the formula: $ECSA = {}^{C_{dl}}/_{C_s}$ (3.3)

where $C_{dl}$ is the double-layer capacitance of the catalyst and $C_s$ is the specific capacitance of the material per unit area under identical electrolyte conditions and is equal to 0.04 mF cm$^{-2}$ in 1.0 M KOH based on reported values. [56] The plot of ECSA *vs* catalyst, in **Figure 3.11b**, shows

that ECSA is highest for NTO-5 after that no increment in ECSA is observed. The $C_{dl}$ and corresponding ECSA values of all catalysts discussed in this study are presented in **Table 3.3**.

**Table 3.3** The $C_{dl}$ and corresponding ECSA values of all the catalysts

| S. No. | Catalyst | $C_{dl}$ (mF cm$^{-2}$) | ECSA (cm$^2$ mg$^{-1}$) |
|---|---|---|---|
| 1 | NTO-0 | 1.12 | 28 |
| 2 | NTO-3 | 1.25 | 47.7 |
| 3 | NTO-5 | 2.24 | 56 |
| 4 | NTO-7.5 | 1.91 | 31.2 |
| 5 | NTO-10 | 0.89 | 22.2 |

Cyclic voltammogram (CV), in **Figure 3.12**, of NTO samples recorded between 1.2 and 1.6 V *vs* RHE consists of a pre-OER reversible redox peak. It is interesting to observe that the anodic peaks of the CV are gradually shifted toward the higher potential with increasing Ti doping in NiO lattice indicating that the doping of Ti increases the polarization of the active $Ni^{2+}/Ni^{3+}$ redox species.

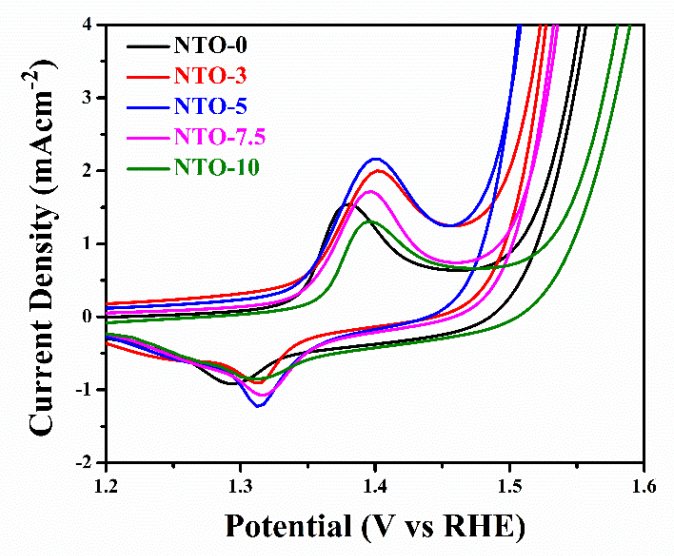


**Figure 3.12.** Cyclic voltammograms of $Ni_{1-2x}Ti_xO$ catalysts with various Ti contents ($0 \le x \le 0.1$) were recorded at a scan rate of 5 mV $s^{-1}$ in 1 M KOH, showing the effect of Ti doping on the pre-OER redox peaks.

$Ti^{4+}$ being a smaller ion with a higher charge has more affinity for electrons than the parent Ni ion. The dopant $Ti^{4+}$ being a stronger Lewis acid, withdraws electrons from Ni and decreases the energy

of antibonding states. [32, 57] This decrease in energy would result in a lower electron energy associated with the redox of M–O bonds, and cause a positive shift in the electrode potential. [32] Previous studies have suggested that the enhanced OER kinetics is accompanied by a positive shift in the potential of a reversible process before the onset of OER. [58-60] The anodic shift of redox potentials in NTO samples caused by the inductive effect of $Ti^{4+}$ led to the enhanced OER activity of NTO-5 than NTO-0. Here we relate the OER activity of metal oxides to the potential of redox processes preceding OER, which also corresponds to the redox of surface metal ion sites, $M^{n+}–OH_{ad}/M^{n+1}–O_{ad}$. The inductive effect of $Ti^{+4}$ ($\chi$ $Ni^{2+/3+}$ = 1.367, 1.695 respectively and $\chi$ $Ti^{4+}$ = 1.730) [57] plays a vital role by increasing the partial positive charge on Ni (in **Figure 3.13**) as also evident from the XPS spectrum. It is also noteworthy, that higher concentrations of cation vacancies in the rock salt structure (NTO-5) act as sites for adsorbing $H_2O$ molecules as evident from the FT-IR spectra (**Figure 3.3c**).

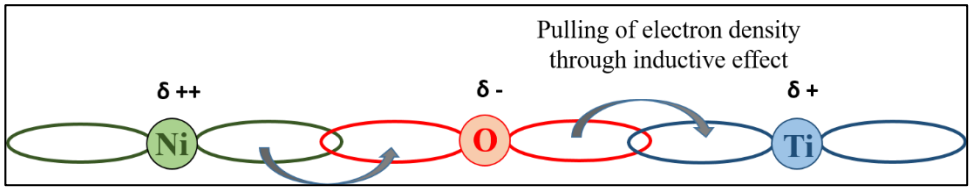


**Figure 3.13**. Pictorial representation of the movement of electron density because of inductive effect, $\chi$ $Ni^{2+/3+}$ = 1.367, 1.695 respectively and $\chi$ $Ti^{4+}$ = 1.730.

The cationic vacancy site acts as the active site to effectively adsorb $H_2O$ molecules, which is a key step for the OER, leading to a significant enhancement in the electrocatalytic activity of OER. [28, 61]

### 3.3.6.2 Comparative OER Study

Commercially available $RuO_2$ (Sigma-Aldrich) was tested as a reference electrocatalyst in the present study to compare its performance with the NTO-5 electrocatalyst, under a similar

experimental condition. The polarization curves of $RuO_2$ along with NTO-5 are plotted in **Figure 3.14** to compare their OER performance. It is observed that the overpotential required for $RuO_2$ to reach the current density of 10 $mAcm^{-2}$ is 332 mV, as reported previously [62] while NTO-5 requires ~304 mV overpotential to reach the same current density. The Tafel slope of NTO-5 and $RuO_2$ was calculated and found to be 67 mV $dec^{-1}$ and 82 mV $dec^{-1}$ respectively, which is in order of their OER performance, as shown in the inset of **Figure 3.14**.

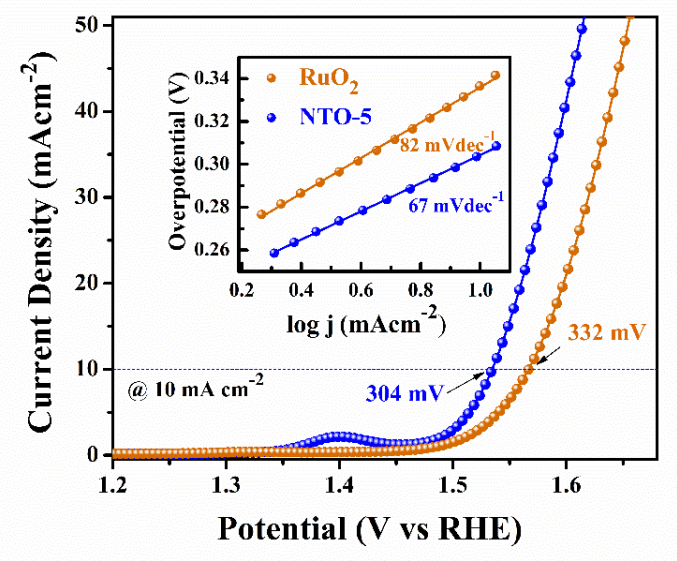


**Figure 3.14.** Comparison of OER performance of NTO-5 with commercial $RuO_2$ as reference catalyst, linear sweep voltammograms recorded at 5 mV $s^{-1}$ in 1 M KOH; inset showing the Tafel plot.

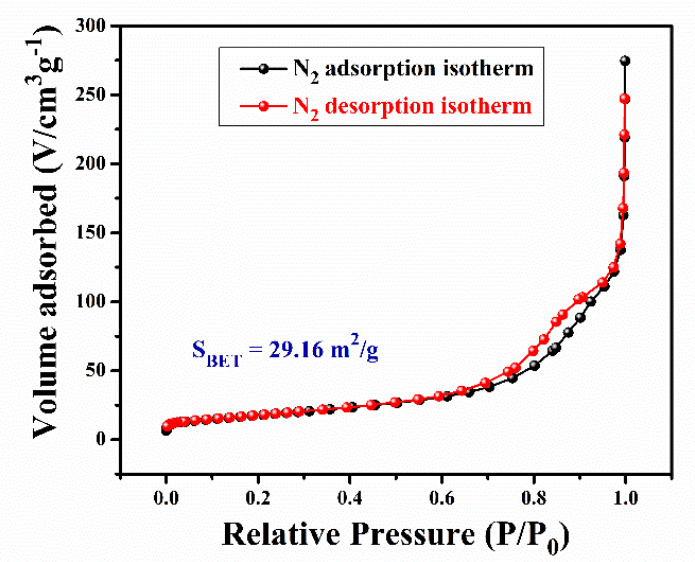


**Figure 3.15** $N_2$ adsorption/desorption isotherm curve of NTO-5.

From BET surface area measurement ($N_2$ adsorption/desorption isotherms) of NTO-5 (see in **Figure 3.15)** the surface area is determined to be 29.16 $m^2/g$ whereas that of commercial $RuO_2$ is 11.38 $m^2/g$. [62]

Under an overpotential of 350 mV, (a fixed overpotential of 350 mV value was chosen based on 10% efficient solar water-splitting devices) [56] the OER current density of NTO-5 reaches 30.4 mA $cm^{-2}$, about 2.5 times higher than commercial $RuO_2$ (12.5 mA $cm^{-2}$). The current density normalized by real available surface area as estimated from BET measurements of the NTO-5 and the benchmark commercial $RuO_2$ catalyst were also calculated under an overpotential of 350 mV and referred to as a specific activity (SA). [63] The SA of NTO-5 is 1.04 mA $cm^{-2}$, comparable to that of $RuO_2$ (1.11 mA $cm^{-2}$), as shown in **Figure 3.17a**. Electric double-layer capacitance ($C_{dl}$) more accurately represents the actual surface area of the material when exposed to the electrolyte during the experiment as compared to the geometrical surface area estimated from the BET method. [64]

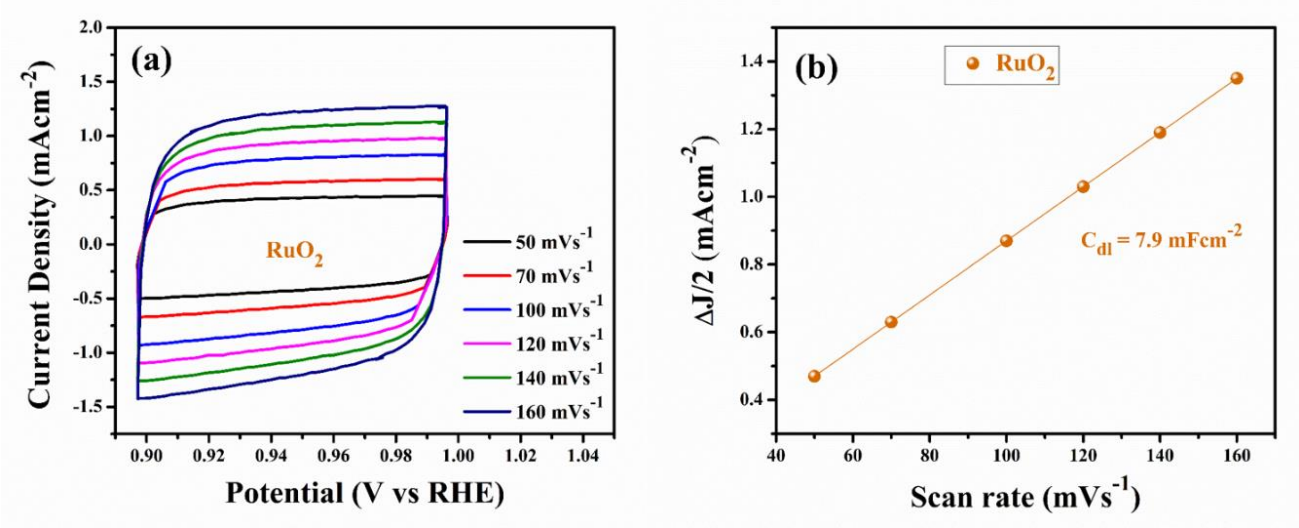


**Figure 3.16** CV measurements in a non-faradic current region (0.9-1.0 V vs. RHE) at scan rates of 50, 100, 120, 140 and 160 mV $s^{-1}$ of **(a)** $RuO_2$ in 1 M KOH & **(b)** plot of capacitive current density difference average (Δj/2) vs the scan rate for $RuO_2$.

The current density normalized by electric double-layer capacitance, designated as EA, of NTO-5 and $RuO_2$, was calculated. $C_{dl}$ of $RuO_2$ was determined to be only 7.9 mF $cm^{-2}$ (in **Figure 3.16**) while that of NTO-5 was 2.24 mF $cm^{-2}$ (as seen in **Figure 3.11e**). The EA for NTO-5 is 13.57 mA $mF^{-1}$, which is ~8 times higher than that of $RuO_2$ (1.61 mA $mF^{-1}$) shown in **Figure 3.17b**, confirming the good activity of NTO-5.

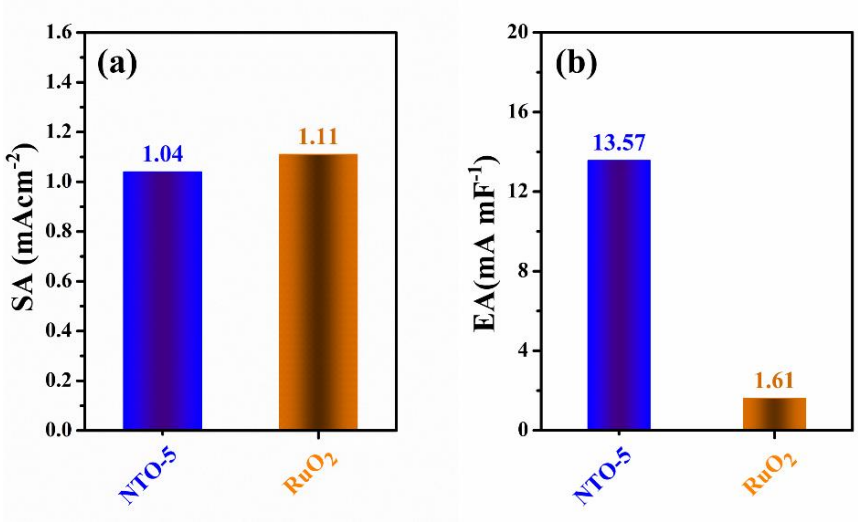


**Figure 3.17**. **(a)** OER activity normalized by BET surface area (SA) and **(b)** electric double-layer capacitance (EA) of NTO-5 and $RuO_2$, respectively, at an overpotential of 350 mV.

### 3.3.6.3 Mott-Schottky Analysis

The excellent catalytic activity of NTO-5 was further verified through the Mott−Schottky plot that provides flat band potential ($E_{fb}$). It is a useful parameter that gives fundamental information about the electrochemical interface potential between the electrode and the electrolyte. [65, 66] The $E_{fb}$ was determined by the intercept of the $1/C^2$ *vs* potential on the x-axis. The Mott−Schottky plot (**Figure 3.18a**) of NTO-0 and NTO-5 measured at a frequency of 100 Hz in the potential window 1.0 and 1.6 V *vs* RHE. The negative slope of the plot shows that NTO-0 and NTO-5 is a *p*-type (hole) semiconductor. From **Figure 3.18a** it was determined that the $E_{fb}$ of NTO-0 is 1.25 V *vs* RHE. For NTO-5 $E_{fb}$ is 1.19 V *vs* RHE, which is less than its onset potential of 1.45 V *vs* RHE in

1 M KOH electrolyte solution. For a *p*-type semiconductor, when $E_{onset} > E_{fb}$, more holes are generated at the electrode region, favoring the OER process. [67, 68]

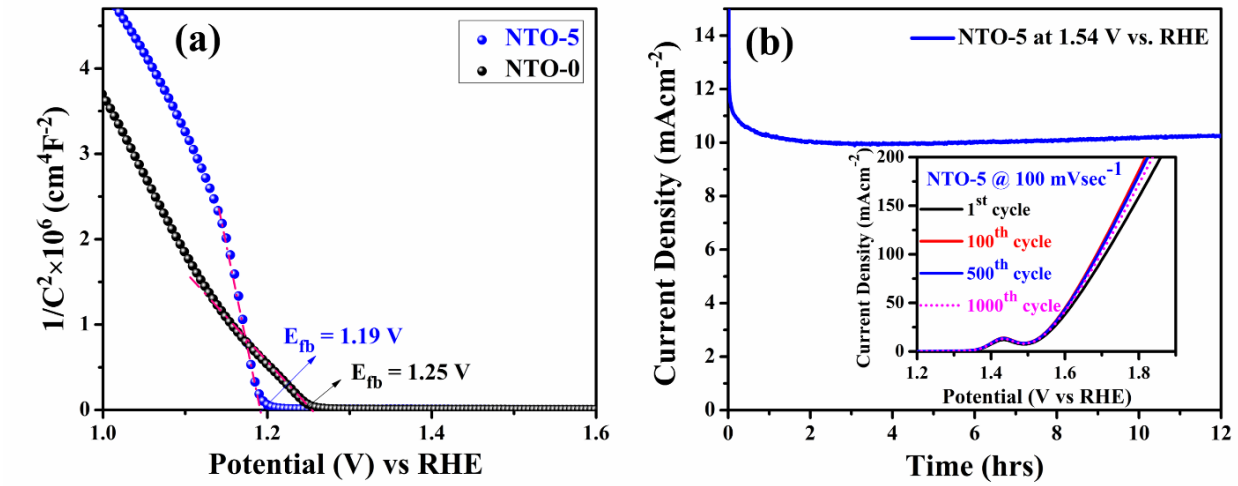


**Figure 3.18. (a)** Mott-Schottky plot for NTO-0 and NTO-5 recorded at a frequency of 100 Hz and **(b)** Chronoamperogram of NTO-5 at an applied potential of 1.54 V *vs*. RHE for 12 hrs; inset shows the linear sweep voltammograms for the 1st, 100th, 500th, and 1000th cycle at a scan rate of 100 mV $s^{-1}$.

### 3.3.6.4 Long-term Stability Test

The stability of electrocatalysts is an important parameter for large-scale water electrolysis applications. [69] The static stability of NTO-5 was evaluated by performing a chronoamperometric (CA) test at 1.54 V *vs* RHE for 12 h, illustrated in **Figure 3.18b**, which shows that NTO-5 exhibits a current density of 10 mA $cm^{-2}$ that increases slightly during the first few hours before reaching a constant value. The stability of the NTO-5 electrocatalyst was also screened by fast scan CV cycling known as accelerated degradation test and prolonged water electrolysis in potentiostatic mode. The accelerated degradation test was carried out by scanning a thousand cycles of CV at a scan rate of 100 $mVsec^{-1}$ in the potential window of 1.0 to 1.8 V *vs* RHE. The inset of **Figure 3.18b** shows the LSV plots of the 1st, 100th, 500th and 1000th cycles of NTO-5, and it was observed that there is only a marginal change in the overpotential at 10 mA

$cm^{-2}$ of the NTO-5 electrocatalyst, indicating its excellent stability in a highly alkaline 1 M aqueous KOH electrolyte.

### 3.3.6.5 Post OER Characterization

The stability of the electrocatalyst NTO-5 after long-term electrochemical cycling was further verified by post–XRD and post-SEM characterizations.

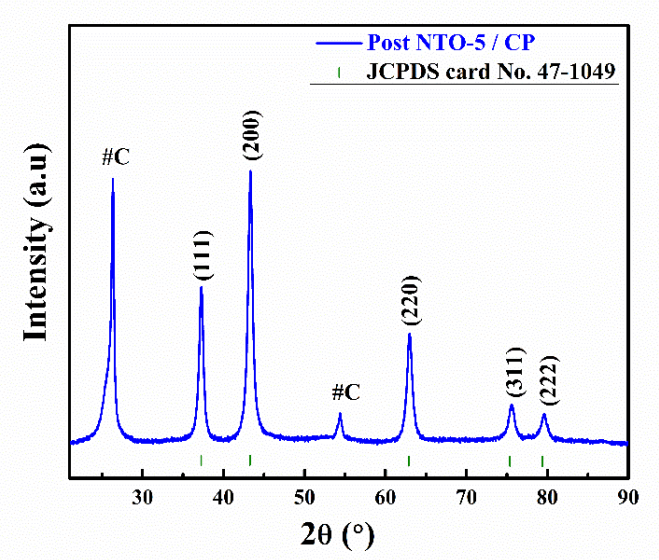


**Figure 3.19** post-OER XRD pattern of NTO-5 electrode.

The XRD analysis conducted after the electrochemical testing on the NTO-5 electrode reveals no changes in the diffraction pattern, except for the presence of peak due to carbon paper, indicating that the structure is retained after testing. The diffraction pattern closely matches the standard cubic phase (space group: Fm-3m) of NiO, indexed well using the (JCPDS no. 47-1049) as shown in **Figure 3.19**. To observe the effect of long-term testing on the morphology of the NTO-5 sample, post-SEM was also performed. HR- SEM images displayed in **Figure 3.20 a** after long-term anodic cycling demonstrate no observable changes in particle size and shape/morphology of the material, and **Figure 3.20 b** shows the EDAX spectrum of NTO-5 post-OER.

Additionally, the post-OER elemental mapping images indicate the uniform presence of Ni, Ti and O elements in the NTO-5 electrode (**Figure 3.20 i–iii**).

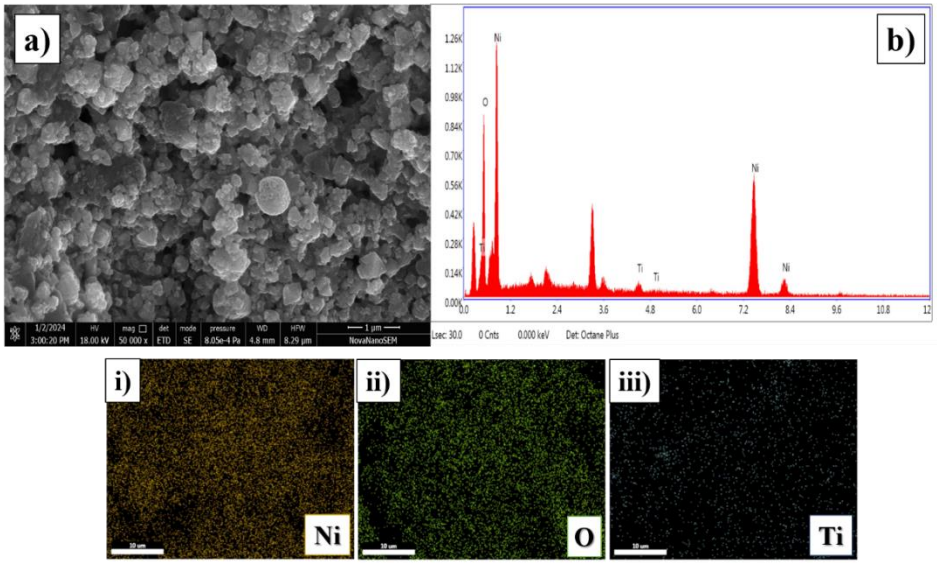


**Figure 3.20 (a)** SEM images, **(b)** energy-dispersive spectrum & **(i-iii)** element mapping of post-OER NTO-5 electrode.

### 3.4 Conclusion

In summary, a series of cubic rock salt NiO structures with 3 to 10% Ti doping ($Ni_{1-2x}Ti_xV_x''O$, $0 < x < 0.1$) have been synthesized by the sol–gel route and investigated for the influence of Ti doping on electrocatalytic activity toward the oxygen evolution reaction (OER). 5% Ti-doped NiO is shown here to be an excellent OER catalyst compared to state-of-the-art $RuO_2$. The origin of the observed higher activity of Ti-doped NiO is due to the formation of cation vacant lattice sites (supported by Raman Studies; **Figure 3.3a, b**) on surfaces for $H_2O$ adsorption and the inductive effect brought about by Ti substitution on Ni site in rock-salt NiO structure. Ti dopant being a stronger Lewis acid as compared to Ni ion, is shown to positively shift the formal redox potentials of $Ni^{2+}/Ni^{3+}$ of the parent active species, as evident from our CVs studies. $Ni^{2+/3+}$ is active site for

OER as Ni(3*d*) orbital are pinned over O(2*p*) orbitals and $Ti^{4+}$ alone don't show any OER activity as O(2*p*) and Ti(3*d*) bands are separated to each other. The $Ti^{4+}$ enhances the ionicity of the Ni–O bond in the lattice through the inductive effect (supported by Raman studies; **Figure 3.3a,** FT-IR; **Figure 3.3c** and XPS; **Figure 3.5b**). Both FT-IR and Raman studies confirm the elongation of Ni–O bond and XPS study confirms high electro-positivity of Ni ions. The higher ionicity of Ni–O leads to a greater overlap between Ni 3*d* and O 2*p* orbital resulting in a higher catalytic activity of the doped catalysts. However, further increase in the Ti concentration leads to a decrease in the concentration of $Ni^{2+/3+}$ redox active sites at the surface due to the formation of a higher concentration of cation vacancy and an increase in concentration of non-active Ti on surfaces. Therefore, an increase in the Ti concentration beyond an optimum level lead to decrease in the OER activity. An optimum concentration of 5% Ti doping leads to the best activity via its inductive effect on the redox potential of the active species, namely $Ni^{2+}/Ni^{3+}$ parent species. Also, this optimum concentration of 5% Ti in NiO shows the best OER activity and $Ni_{0.9}Ti_{0.05}O$ depicts a Tafel slope of 67 mV $dec^{-1}$ and an overpotential of 304 mV at a current density of 10 mA $cm^{-2}$ confirming a comparable electrocatalytic OER activity to that of the commercial benchmark $RuO_2$ catalyst, measured under similar experimental conditions.

## 3.5 References


1. You, B.; Sun, Y. Innovative strategies for electrocatalytic water splitting. *Acc. Chem. Res.,* **2018**, *51*, 1571-1580.
2. Zheng, Y.; Jiao, Y.; Jaroniec, M.; Qiao, S. Z. Advancing the electrochemistry of the hydrogen-evolution reaction through combining experiment and theory. *Angew. Chem., Int. Ed.,* **2015**, *54*, 52-65.
3. Gupta, A.; Kushwaha, V.; Mondal, R.; Singh, A. N.; Prakash, R.; Mandal, K. D.; Singh, P. $SrFeO_{3-\delta}$ : a novel $Fe^{4+} \leftrightarrow Fe^{2+}$ redox-mediated pseudocapacitive electrode in aqueous electrolyte. *Phys. Chem. Chem. Phys.,* **2022**, *24*, 11066-11078.
4. Wan, D. Y.; Fan, Z. Y.; Dong, Y. X.; Baasanjav, E.; Jun, H. B.; Jin, B.; Jin, E. M.; Jeong, S. M. Effect of metal (Mn, Ti) doping on NCA cathode materials for lithium-ion batteries. *J. Nanomater*. **2018**, *2018*, 1-9.
5. Soni, V.; Singh, A. N.; Singh, P.; Gupta, A. Photocatalytic dye-degradation activity of nano-crystalline $Ti_{1-x}M_xO_{2-\delta}$ (M= Ag, Pd, Fe, Ni and x = 0, 0.01) for water pollution abatement. *RSC Adv.,* **2022**, *12*, 18794-18805.
6. Mondal, R.; Ratnawat, H.; Kumar, S.; Kumar, A.; Singh, P. Ni stabilized rock-salt structured CoO; $Co_{1-x}Ni_x$ O: tuning of $e_g$ electrons to develop a novel OER catalyst. *RSC Adv.,* **2020**, *10*, 17845-17853.
7. Yang, M. Q.; Wang, J.; Wu, H.; Ho, G. W. Noble metal-free nanocatalysts with vacancies for electrochemical water splitting. *Small*, **2018**, *14*, 1703323.
8. Song, J.; Wei, C.; Huang, Z. F.; Liu, C.; Zeng, L.; Wang, X.; Xu, Z. J. A review on fundamentals for designing oxygen evolution electrocatalysts. *Chem. Soc. Rev.,* **2020**, *49*, 2196-2214.
9. Sun, H.; Xu, X.; Kim, H.; Jung, W.; Zhou, W.; Shao, Z. Electrochemical water splitting: Bridging the gaps between fundamental research and industrial applications. *Energy Environ. Mater.,* **2023**, *6*, e12441.
10. Moschkowitsch, W.; Dhaka, K.; Gonen, S.; Attias, R.; Tsur, Y.; Caspary Toroker, M.; Elbaz, L. Ternary NiFeTiOOH catalyst for the oxygen evolution reaction: Study of the effect of the addition of Ti at different loadings. *ACS Catal.,* **2020**, *10*, 4879-4887.
11. Yang, M. Q.; Wang, J.; Wu, H.; Ho, G. W. Noble metal-free nanocatalysts with vacancies for electrochemical water splitting. *Small*, **2018**, *14*, 1703323.

12. Pebley, A. C.; Decolvenaere, E.; Pollock, T. M.; Gordon, M. J. Oxygen evolution on Fe-doped NiO electrocatalysts deposited via microplasma. *Nanoscale,* **2017**, *9*, 15070-15082.
13. Gong, M.; Li, Y.; Wang, H.; Liang, Y.; Wu, J. Z.; Zhou, J.; Wang, J.; Regier, T.; Wei, F.; Dai, H. An advanced Ni–Fe layered double hydroxide electrocatalyst for water oxidation. *J. Am. Chem. Soc.,* **2013**, *135*, 8452-8455.
14. Guiet, A.; Huan, T. N.; Payen, C.; Porcher, F.; Mougel, V.; Fontecave, M.; Corbel, G. Copper-substituted $NiTiO_3$ ilmenite-type materials for oxygen evolution reaction. *ACS Appl. Mater. Interfaces,* **2019**, *11*, 31038-31048.
15. Rodríguez-Hernández, F.; Tranca, D. C.; Martínez-Mesa, A.; Uranga-Piña, L.; Seifert, G. Water splitting on transition metal active sites at $TiO_2$-based electrodes: a small cluster study. *J. Phys. Chem. C,* **2016**, *120,* 25851-25860.
16. Han, J.; Choi, H.; Lee, G.; Tak, Y.; Yoon, J. Electrochemical Activity of a Blue Anatase $TiO_2$ Nanotube Array for the Oxygen Evolution Reaction in Alkaline Water Electrolysis. *J. Electrochem. Sci. Technol.,* **2016**, *7*, 76-81.
17. Yang, Y.; Kao, L. C.; Liu, Y.; Sun, K.; Yu, H.; Guo, J.; Liou, S. Y.H.; Hoffmann, M. R. Cobalt-doped black $TiO_2$ nanotube array as a stable anode for oxygen evolution and electrochemical wastewater treatment. *ACS Catal.,* **2018**, *8*, 4278-4287.
18. Zhao, Y.; Jia, X.; Chen, G.; Shang, L.; Waterhouse, G. I.; Wu, L. Z.; Tung, C. H.; O'Hare, D.; Zhang, T. Ultrafine NiO nanosheets stabilized by $TiO_2$ from monolayer NiTi-LDH precursors: an active water oxidation electrocatalyst. *J. Am. Chem. Soc.,* **2016**, *138*, 6517-6524.
19. Nai, J.; Lu, Y.; Yu, X. Y. Formation of Ti–Fe mixed sulfide nanoboxes for enhanced electrocatalytic oxygen evolution. *J. Mater. Chem. A,* **2018**, *6*, 21891-21895.
20. Zhang, P. F.; Zhang, J. Y.; Sheng, T.; Lu, Y. Q.; Yin, Z. W.; Li, Y. Y.; Peng, X. X.; Zhou, Y.; Li, J. T.; Wu, Y. J.; Lin, J. X.; Xu, B. B.; Qu, X. M.; Huang, L.; Sun, S. G.; Sun, S. G. Synergetic effect of Ru and NiO in the electrocatalytic decomposition of $Li_2CO_3$ to enhance the performance of a Li-$CO_2$/$O_2$ battery. *ACS Catal.,* **2019**, *10*, 1640-1651.
21. Wen, C. K.; Xin, Y. Q.; Chen, S. C.; Chuang, T. H.; Chen, P. J.; Sun, H. Comparison of microstructural and optoelectronic properties of NiO: Cu thin films deposited by ion-beam assisted rf sputtering in different gas atmospheres. *Thin Solid Films,* **2019**, *677*, 103-108.

22. Yang, M.; Shi, Z.; Feng, J.; Pu, H.; Li, G.; Zhou, J.; Zhang, Q. Copper doped nickel oxide transparent p-type conductive thin films deposited by pulsed plasma deposition. *Thin Solid Films*, **2011**, *519*, 3021-3025.
23. Yin, Y.; Zhang, Y.; Gao, T.; Yao, T.; Zhang, X.; Han, J.; Wang, X.; Zhang, Z.; Xu, P.; Zhang, P.; Cao, X.; Song, B.; Jin, S. Synergistic Phase and Disorder Engineering in 1T-$MoSe_2$ Nanosheets for Enhanced Hydrogen-Evolution Reaction. *Adv. Mater*. **2017**, *29 (28)*, 1700311.
24. Bolar, S.; Shit, S.; Kumar, J. S.; Murmu, N. C.; Ganesh, R. S.; Inokawa, H.; Kuila, T. Optimization of Active Surface Area of Flower Like $MoS_2$ Using V-Doping towards Enhanced Hydrogen Evolution Reaction in Acidic and Basic Medium. *Appl. Catal., B* **2019**, *254*, 432−442.
25. Zhu, J. Q.; Ren, Z. Y.; Du, S. C.; Xie, Y.; Wu, J.; Meng, H. Y.; Xue, Y. Z.; Fu, H. G. Co-Vacancy-Rich $Co_{1-x}S$ Nanosheets Anchored on rGO for High-Efficiency Oxygen Evolution. *Nano Res*. **2017**, *10 (5)*, 1819−1831
26. Wang, L.; Peng, C.; Lin, H.; Zhao, B. Unraveling the role of defects in electrocatalysts for water splitting: recent advances and perspectives. *Energy & Fuels.*, **2022**, *36(19)*, 11660-11690.
27. Zhao, B.; Zhang, L.; Zhen, D.; Yoo, S.; Ding, Y.; Chen, D.; Chen, Y.; Zhang, Q.; Doyle, B.; Xiong, X.; Liu, M. A Tailored Double Perovskite Nanofiber Catalyst Enables Ultrafast Oxygen Evolution. *Nat. Commun*. **2017**, *8 (1)*, 14586.
28. Liu, Y.; Cheng, H.; Lyu, M.; Fan, S.; Liu, Q.; Zhang, W.; Zhi, Y.; Wang, C.; Xiao, C.; Wei, S.; Ye, B.; Xie, Y. Low overpotential in vacancy-rich ultrathin $CoSe_2$ nanosheets for water oxidation. *J. Am. Chem. Soc.*, **2014**, *136*, 15670-15675.
29. Lee, H. J.; Back, S.; Lee, J. H.; Choi, S. H.; Jung, Y.; Choi, J. W. Mixed transition metal oxide with vacancy-induced lattice distortion for enhanced catalytic activity of oxygen evolution reaction. *ACS Catal.*, **2019**, *9*, 7099-7108.
30. Cai, Z.; Bi, Y.; Hu, E.; Liu, W.; Dwarica, N.; Tian, Y.; Li, X.; Kuang, Y.; Li, Y.; Yang, X. Q.; Wang, H.; Sun, X. Single-crystalline ultrathin $Co_3O_4$ nanosheets with massive vacancy defects for enhanced electrocatalysis. *Adv. Energy Mater.*, **2018**, *8*, 1701694.
31. Chen, H., Fu, W., Geng, Z., Zeng, J., Yang, B. Inductive effect as a universal concept to design efficient catalysts for $CO_2$ electrochemical reduction: electronegativity difference makes a difference. *J. Mater. Chem. A*, **2021,** *9*, 4626-4647.

32. Kuznetsov, D. A.; Han, B.; Yu, Y.; Rao, R. R.; Hwang, J.; Román-Leshkov, Y.; Shao-Horn, Y. Tuning redox transitions via inductive effect in metal oxides and complexes, and implications in oxygen electrocatalysis. *Joule*, **2018**, *2*, 225-244.
33. Peng, J.; Yuan, S.; Cai, B.; Giordano, L.; Román-Leshkov, Y.; Shao-Horn, Y. Leveraging the Inductive Effect to Promote Oxygen Evolution on Oxides and Metal Hydroxide-Organic Frameworks. In *Electrochemical Society Meeting Abstracts 242*, **2022**, *46*, 1710-1710
34. Kuznetsov, D. A.; Peng, J.; Giordano, L.; Roman-Leshkov, Y.; Shao-Horn, Y. Bismuth substituted strontium cobalt perovskites for catalyzing oxygen evolution. *J. Phys. Chem. C*, **2020** *124(12)*, 6562-6570.
35. Lin, Y.; Wang, Y.; Wang, H.; Wang, J.; Wu, X.; Hofmann, J. P.; Gorni, G.; Peña O'Shea, Victor A., de la; Oropeza, F. E.; Zhang, K. H. Inductive effect of Ti-doping in $Fe_2O_3$ enhances the photoelectrochemical water oxidation. *Sci. China Chem*, **2023** *66(7)*, 2091-2097.
36. Soni, V.; Jaiswal, S.; Singh, P.; Gupta, A. Aluminum-Doped Lithium-Vacant Layered $Li_{1-x}Cr_{1-x}Al_xO_2$: A Potentially Active Electrocatalyst for the Oxygen Evolution Reaction. *ACS Appl. Energy Mater.* **2024**, *7*(8), 3175-3186.
37. Kushwaha, V.; Gupta, A.; Choudhary, R. B.; Mandal, K. D.; Mondal, R.; Singh, P. Nanocrystalline β-NiS: a redox-mediated electrode in aqueous electrolyte for pseudocapacitor/supercapacitor applications. *Phys. Chem. Chem. Phys*., **2023**, *25*, 555-569.
38. Sharma, K. R., & Negi, N. S. Significant improvement in the structural, microstructural, and room-temperature magnetic properties of Fe-doped NiO nanoparticles prepared by the solution combustion method. *J. Mater. Sci.: Mater. Electron.*, **2022**, *33(28)*, 22518-22540
39. Sharma, K. R.; Negi, N. S. Doping effect of cobalt on various properties of nickel oxide prepared by solution combustion method. *J. Supercond. Nov. Magn.*, **2021**, *34*(2), 633-645.
40. Prasad, N.; Veillon, F.; Kumar, P R.; Prellier, W. Raman spectroscopic and magnetic properties of Europium doped nickel oxide nanoparticles prepared by microwave-assisted hydrothermal method. *J. Alloys Compd.*, **2021**, *858*, 157639.
41. Bhanuchandar, S.; Vinothkumar, G.; Arunkumar, P.; Sribalaji, M.; Keshri, A. K.; Babu, K. S. Unravelling the role of cationic $Ni^{2+}$ vacancies and $Ni^{3+}$ ions in non-stoichiometric NiO: breakdown of anti-ferromagnetic ordering and large exchange bias. *J. Mater. Sci.*, **2023**, *58*(32), 13136-13153.

42. Elkamel, I. B.; Hamdaoui, N.; Mezni, A.; Ajjel, R.; & Beji, L. High responsivity and 1/f noise of an ultraviolet photodetector based on Ni doped ZnO nanoparticles. *RSC Adv.*, **2018**, *8*, 32333-32343.
43. Bhoye, M.; Pansambal, S.; Basnet, P.; Lin, K. Y. A.; Gutierrez-Mercado, K. Y.; Pérez-Larios, A.; Chauhan, A.; Ghotekar, S. Eco-Friendly Synthesis of Ni/NiO Nanoparticles Using Gymnema sylvestre Leaves Extract for Antifungal Activity. *J. Compos. Sci.*, **2023**, *7*, 105.
44. Ngo, Y. L. T.; Hur, S. H. Low-temperature $NO_2$ gas sensor fabricated with NiO and reduced graphene oxide hybrid structure. *Mater. Res. Bull.*, **2016**, *84*, 168-176.
45. Bidier, S. A.; Hashim, M. R.; Bououdina, M. Structural and optical characteristics of Ti-doped ZnO nanorods deposited by simple chemical bath deposition. *J Mater Sci: Mater Electron.*, **2017**, *28*, 11178-11185.
46. Hefnawy, M. A.; Fadlallah, S. A.; El-Sherif, R. M.; Medany, S. S. Synergistic effect of Cu-doped NiO for enhancing urea electrooxidation: Comparative electrochemical and DFT studies. *J. Alloys Compd*., **2022**, *896*, 162857.
47. Dubey, P.; Kaurav, N.; Devan, R. S.; Okram, G. S.; Kuo, Y. K. The effect of stoichiometry on the structural, thermal and electronic properties of thermally decomposed nickel oxide. *RSC Adv*., **2018**, *8*, 5882-5890.
48. Xu, X.; Zhang, H.; Tong, Y.; Sun, Y.; Fang, X.; Xu, J.; Wang, X. Tuning $Ni^{3+}$ quantity of NiO via doping of cations with varied valence states: The key role of $Ni^{3+}$ on the reactivity. *Appl. Surf. Sci.*, **2021**, *550*, 149316.
49. Soni, V.; Jaiswal, S.; Nigam, K. G.; Singh, P.; Gupta, A. Nickel Doped Lithium-Vacant Layered $Li_yCr_{1-x}Ni_xO_2$: A Potentially Active Electrocatalyst for Oxygen Evolution Reaction. **2024**, *J. Mater. Chem. A*. 12, 19212-19226.
50. Murcia-Lopez, S.; Moschogiannaki, M.; Binas, V.; Andreu, T.;́ Tang, P.; Arbiol, J.; Biendicho, J. J.; Kiriakidis, G.; Morante, J. R. Insights into the Performance of $Co_xNi_{1-x}TiO_3$ Solid Solutions as Photocatalysts for Sun-Driven Water Oxidation. *ACS Appl. Mater. Interfaces,* **2017**, *9*, 40290−40297.
51. Xie, W.; Li, R.; Xu, Q. Enhanced photocatalytic activity of Se-doped TiO2 under visible light irradiation. *Sci. Reports*, **2018** *8*(1), 8752.

52. Gupta, A.; Kumar, A.; Waghmare, U. V.; Hegde, M. S. Origin of activation of lattice oxygen and synergistic interaction in bimetal-ionic $Ce_{0.89}Fe_{0.1}Pd_{0.01}O_{2-\delta}$ catalyst. *Chem. mater.*, **2009**, *21*(20), 4880-4891.
53. Scofield, J. H. Hartree-Slater subshell photoionization cross sections at 1254 and 1487 eV. *J. Electron Spectrosc. Relat. Phenom.* **1976**, 8, 129−137.
54. Penn, D. R. Quantitative chemical analysis by ESCA. *J. Electron Spectrosc. Relat. Phenom.* **1976**, 9, 29−40.
55. Soni, V.; Mondal, R.; Singh, A. N.; Singh, P.; Gupta, A. Dumbbell Defect Containing Chromium-Rich Lithium-Vacant Layered $Li_yCr_{1-x}Fe_xO_2$ ($y\leq 1$, $0\leq x\leq 0.2$): An Unexplored and Highly Efficient Electrocatalyst for the Oxygen Evolution Reaction. *ACS Appl. Energy Mater.*, **2023**, *6*(3), 1308-1320.
56. McCrory, C. C. L.; Jung, S.; Peters, J. C.; Jaramillo, T. F. Benchmarking heterogeneous electrocatalysts for the oxygen evolution reaction. *J. Am. Chem. Soc.* **2013**, *135*, 16977-16987.
57. Li, K.; Xue, D. Estimation of electronegativity values of elements in different valence states. *J. Phys. Chem. A*, **2006**, *110*, 11332-11337.
58. Enman, L. J.; Burke, M. S.; Batchellor, A. S.; Boettcher, S. W. Effects of intentionally incorporated metal cations on the oxygen evolution electrocatalytic activity of nickel (oxy) hydroxide in alkaline media. *ACS Catal*., **2016**, *6*, 2416-2423.
59. Han, X.; Wang, B.; Yang, C.; Meng, G.; Zhao, R.; Hu, Q.; Triana, O.; Iqbal, M.; Li, Y.; Han, A.; Liu, J. Inductive effect in Mn-doped NiO nanosheet arrays for enhanced capacitive and highly stable hybrid supercapacitor. *ACS Appl. Energy Mater.*, **2019**, *2*, 2072-2079.
60. Herbert, D. E.; Lionetti, D.; Rittle, J.; Agapie, T. Heterometallic triiron-oxo/hydroxo clusters: effect of redox-inactive metals. *J. Am. Chem. Soc*., **2013**, *135*, 19075-19078.
61. Lu, Z.; Zhu, W.; Yu, X.; Zhang, H.; Li, Y.; Sun, X.; Wang, X.; Wang, H.; Wang, J.; Luo, J.; Lei, X.; Jiang, L. Ultrahigh hydrogen evolution performance of under-water "superaerophobic" $MoS_2$ nanostructured electrodes. *Adv. Mater.*, **2014**, *26*, 2683-2687.
62. Anantharaj, S.; Reddy, P. N.; Kundu, S. Core-oxidized amorphous cobalt phosphide nanostructures: an advanced and highly efficient oxygen evolution catalyst. *Inorg. Chem.*, **2017**, *56*, 1742-1756.

63. Zhu, K.; Wu, T.; Zhu, Y.; Li, X.; Li, M.; Lu, R.; Wang, J.; Zhu, X.; Yang, W. Layered Fe-substituted $LiNiO_2$ electrocatalysts for high-efficiency oxygen evolution reaction. *ACS Energy Lett.*, **2017**, *2*, 1654-1660.
64. Anantharaj, S.; Ede, S. R.; Karthick, K.; Sankar, S. S.; Sangeetha, K.; Karthik, P. E.; Kundu, S. Precision and correctness in the evaluation of electrocatalytic water splitting: revisiting activity parameters with a critical assessment. *Energy Environ. Sci.*, **2018**, *11*, 744-771.
65. Bockris, J. O. M.; Otagawa, T. The electrocatalysis of oxygen evolution on perovskites. *J. Electrochem. Soc.*, **1984**, *131*, 290-302.
66. Jaiswal, S.; Mondal, R.; Kushwaha, V.; Gupta, A.; Singh, P. Tuning of Redox Energy of Transition-Metal Ions through the Utilization of Interlayer Potentials in Layered Perovskites: Development of a Titanium-Based Superior HER Catalyst in an Acidic Medium. *ACS Appl. Energy Mater.*, **2023**, *6*, 7323-7334.
67. Mondal, R.; Ratnawat, H.; Mukherjee, S.; Gupta, A.; Singh, P. Investigation of the role of Sr and development of superior Sr-doped hexagonal $BaCoO_{3-\delta}$ perovskite bifunctional OER/ORR catalysts in alkaline media. *Energy Fuels*, **2022**, *36*, 3219-3228.
68. Cheng, X.; Fabbri, E.; Yamashita, Y.; Castelli, I. E.; Kim, B.; Uchida, M.; Haumont, R.; Puente-Orench, I.; Schmidt, T. J. Oxygen evolution reaction on perovskites: A multieffect descriptor study combining experimental and theoretical methods. *ACS Catal.*, **2018**, *8*, 9567-9578.
69. Anantharaj, S.; Ede, S. R.; Sakthikumar, K.; Karthick, K.; Mishra, S.; Kundu, S. Recent trends and perspectives in electrochemical water splitting with an emphasis on sulfide, selenide, and phosphide catalysts of Fe, Co, and Ni: A review. *ACS Catal.*, **2016**, *6*, 8069-8097.